

Superconducting Acoustogalvanic Effect in Twisted Transition Metal Dichalcogenides

Tsugumi Matsumoto,^{1,*} Ryotaro Sano,^{1,2} Youichi Yanase,¹ and Akito Daido^{1,3}

¹*Department of Physics, Graduate School of Science, Kyoto University, Kyoto 606-8502, Japan*

²*Institute of Solid State Physics, University of Tokyo, Kashiwa 277-8581, Japan*

³*Department of Physics, Hong Kong University of Science and Technology, Clear Water Bay, Hong Kong, China*

(Dated: September 11, 2025)

Two-dimensional van der Waals superconductors are attracting much attention owing to their rich phase diagrams including possible unconventional superconductivity. However, they suffer from a lack of reliable methods for identifying their nontrivial pairing symmetries and quantum geometry. In this study, we propose nonlinear responses driven by surface acoustic waves as a novel probe to access exotic Bogoliubov quasiparticles in such superconductors. Our approach is particularly suitable for addressing the superconducting gap structure as the gap energies in these systems typically lie within the frequency range of surface acoustic waves, and thus paves the way toward the experimental identification of exotic superconducting states especially in low- T_c superconductors.

Introduction.— The recent discovery of twisted multilayer van der Waals (vdW) superconductors with the honeycomb structure, exemplified by magic angle twisted bilayer graphene (MATBG) [1] and twisted WSe₂ (tWSe₂) [2, 3], has opened avenues for realizing various exotic superconducting states that have long been sought after. Particularly in tWSe₂, chiral and nematic superconductivity—which spontaneously break time-reversal and rotational symmetries, respectively—are promising candidates for its observed superconducting state [4–7]. Towards their experimental identification, it is essential to clarify the wave-function properties of Cooper pairs and Bogoliubov quasiparticles, namely their symmetry and quantum geometry. However, conventional probes such as optical responses and heat transport face difficulty in accessing these properties due to extremely low critical temperatures as well as the two-dimensional nature. Therefore, developing advanced measurement methods more suitable for atomically thin vdW superconductors is highly desired.

Nonlinear responses have recently established their profound connections to the symmetry and quantum geometry inherent in normal-state Bloch electrons [8, 9]. This concept has now been extended to superconducting states with particular emphasis on nonlinear optical responses [10–17]. By activating the hidden quantum-geometric properties of Bogoliubov quasiparticles, nonlinear responses may provide a powerful tool for studying exotic superconducting states. However, the electromagnetic fields suffer from a fundamental limitation intrinsic to superconductors: the coupling between the vector potential and momentum enters with opposite signs in the particle and hole sectors. This fact sharply contrasts with the normal-state counterpart, and thus prevents nonlinear optical responses from directly capturing the quantum geometry of Bogoliubov quasiparticles in momentum space, which is most relevant in condensed matter physics.

Surface acoustic waves (SAWs) are highly directional mechanical vibrations that propagate along the surface

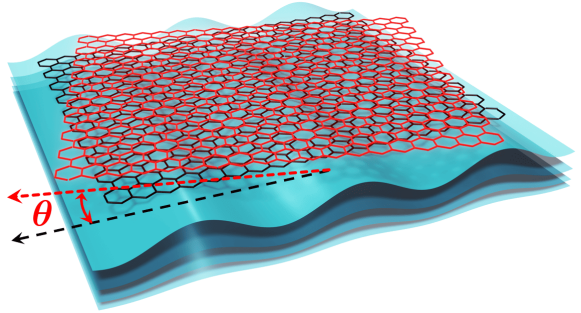


FIG. 1. Schematics of the superconducting acoustogalvanic effect in twisted vdW materials with a twist angle θ . A spatial modulation of the hopping energies due to strain mimics the role of artificial gauge fields for Bogoliubov quasiparticles in a honeycomb lattice.

of elastic media. SAWs serve as a vibrational probe at the nanoscale, offering a compelling platform for simultaneously modulating materials via surfing carriers in 2D materials through piezoelectric and strain fields [18–22]. Specifically in honeycomb systems, a spatial modulation of the hopping energies due to strain mimics the role of artificial gauge fields [23–31], exerting a driving force even on charge-neutral quasiparticles [32–37]. Therefore, the strain-induced gauge fields have the potential to replace the role of electromagnetic fields and temperature gradients in the study of atomically thin vdW materials, owing to their remarkable mechanical flexibility. Furthermore, these strain gauge fields work at the two valley points in the opposite direction, thereby activating the valley degrees of freedom (DOF). This valley-contrasting nature offers a distinct advantage in overcoming the electromagnetic limitation in honeycomb superconductors. It enables direct access to quantum geometry, especially in systems where Cooper pairs are formed between electrons located at the opposite valley points.

In this Letter, we propose the *superconducting acoustogalvanic effect*—a nonlinear response driven by SAWs—as a novel probe of the pairing symmetry and quan-

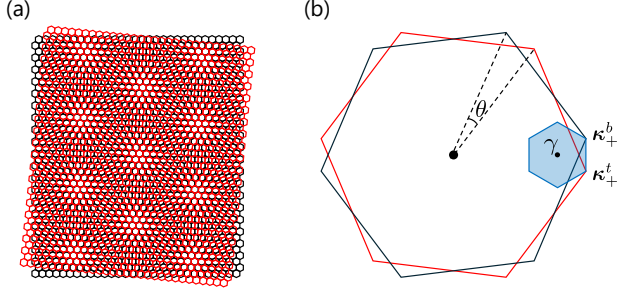


FIG. 2. Schematics of (a) the moiré superlattice and (b) the corresponding reciprocal space with a twist angle θ . The red and black sheets represent the top and bottom layers, respectively. The blue area is the folded moiré Brillouin zone.

tum geometry of Bogoliubov quasiparticles in two-dimensional honeycomb superconductors including those formed with a twisted bilayer (Fig. 1). The unique combination of mechanical tunability and valley-contrasting pseudo-gauge fields elevates SAWs as a promising tool for probing the symmetry and quantum-geometry aspects in atomically thin superconductors. In particular, we focus on inter-valley pairing in tWSe₂, where the valley-contrasting nature of strain fields allows selective activation of quantum-geometric responses that are otherwise hidden in conventional electromagnetic probes. We show that SAWs can induce a pronounced nonlinear response, tightly linked to the underlying quantum geometry of the superconducting state, and further discuss its potential as a remarkable tool for investigating exotic superconducting states in vdW materials.

Model.— To investigate SAWs responses in honeycomb superconductors, we examine an AA-stacked bilayer WSe₂ with a small twist angle θ [Fig. 2(a)]. We begin with the standard continuum model [38] defined in the moiré Brillouin zone (MBZ) as depicted in Fig. 2(b),

$$\hat{H}_\tau = \begin{pmatrix} H_{\tau,b}(\hat{\mathbf{k}}) + \Delta_b(\hat{\mathbf{r}}) & T_\tau(\hat{\mathbf{r}}) \\ T_\tau^\dagger(\hat{\mathbf{r}}) & H_{\tau,t}(\hat{\mathbf{k}}) + \Delta_t(\hat{\mathbf{r}}) \end{pmatrix}, \quad (1)$$

where $\tau = \pm$ and $l = b/t = \pm$ denote the valley and layer DOF. Owing to the spin-orbit coupling, the spin of the $\tau = \pm$ valley is locked to \uparrow and \downarrow , respectively, and are kept implicit. Here, $H_{\tau,l}(\hat{\mathbf{k}})$ is the Hamiltonian of each monolayer, and $\Delta_l(\hat{\mathbf{r}})$ and $T_\tau(\hat{\mathbf{r}})$ are intralayer and interlayer potentials, respectively. These components are given by $H_{\tau,l}(\hat{\mathbf{k}}) = -\frac{\hbar^2}{2m^*}(\hat{\mathbf{k}} - \boldsymbol{\kappa}_{\tau,l})^2 - l\frac{V_z}{2} - \mu$, $\Delta_l(\hat{\mathbf{r}}) = V \sum_{j=1,2,3} e^{i(\mathbf{g}_j \cdot \hat{\mathbf{r}} + l\psi)} + \text{h.c.}$, $T_\tau(\hat{\mathbf{r}}) = w(1 + e^{+i\tau\mathbf{g}_2 \cdot \hat{\mathbf{r}}} + e^{-i\tau\mathbf{g}_3 \cdot \hat{\mathbf{r}}})$, where $m^* = 0.43m_e$ is the effective mass, μ is the chemical potential, and $\boldsymbol{\kappa}_{\tau,l} = [4\pi/3L_M](\sqrt{3}/2, l/2)$ are the momentum shifts. Here, the moiré lattice constant and the reciprocal lattice vectors in the MBZ are given by, $L_M = a_0/[2 \sin \frac{\theta}{2}]$ and $\mathbf{g}_j = \frac{4\pi}{\sqrt{3}L_M} \left(\cos \frac{2(j-1)\pi}{3}, \sin \frac{2(j-1)\pi}{3} \right)$. Throughout this Letter, we set the parameters: $(\theta, \psi, w, V, V_z, \mu) =$

$(5^\circ, 128^\circ, 18 \text{ meV}, 9 \text{ meV}, 43.75 \text{ meV}, -13 \text{ meV})$ [3, 39, 40] and the lattice constant of each monolayer $a_0 = 3.317 \text{ \AA}$.

To describe the superconducting state, we construct the unstrained Bogoliubov-de Gennes (BdG) Hamiltonian,

$$\hat{H}_{\text{BdG}} = \begin{pmatrix} \hat{H}_+ & \Delta(\hat{\mathbf{k}}) \\ \Delta^\dagger(\hat{\mathbf{k}}) & -\hat{H}_-^T \end{pmatrix}, \quad (2)$$

whose eigenstates and eigenvalues are evaluated with keeping only the first-order interlayer coupling to calculate response functions [41]. Various pairing symmetries have been proposed for tWSe₂, including chiral/nematic *p*- and *d*-wave states [4–7]. In the main text of this Letter, we consider both the chiral and nematic *d*-wave states as promising candidates of superconductivity in tWSe₂ [4, 5]. The corresponding order parameters are given by $\Delta(\mathbf{k}) = \Delta(T)(k_x^2 - k_y^2 + 2ik_xk_y)/k^2$ and $\Delta(T)(k_x^2 - k_y^2)/k^2$, respectively, with $k = |\mathbf{k}|$. The gap amplitude is assumed to follow a phenomenological temperature dependence $\Delta(T) = \Delta_0 \tanh \left[1.74 \sqrt{\frac{T_c}{T} - 1} \right]$ with $\Delta_0 = 1.76 k_B T_c$, where $T_c = 0.426 \text{ K}$ is the critical temperature for the twist angle 5.0° [3]. The chiral/nematic *p*-wave state [6, 7] is discussed in the Supplemental Material (SM) and shown to exhibit qualitatively similar behavior to the *d*-wave states.

SAWs and pseudo-gauge fields.— To discuss superconducting SAWs responses, we consider SAWs propagating along the surface of the tWSe₂ [see Fig. 1], introducing a spatio-temporally periodic strain in the crystal lattice. In particular, we focus on the Rayleigh-type SAWs, which can be excited under traction-free boundary conditions on piezoelectric substrates [42]. The Rayleigh-type SAWs propagating on the surface of piezoelectric substrates in the *xy* plane are described by the displacement field $\mathbf{u}(\mathbf{r}, t) = \text{Re} \left[(u_L \hat{\mathbf{Q}} + iu_z \hat{\mathbf{z}}) e^{i(\mathbf{Q} \cdot \mathbf{r} - \Omega t)} \right]$. Here, u_L and u_z are the longitudinal and out-of-plane components, $\mathbf{Q} = Q \hat{\mathbf{Q}} = Q(\cos \varphi, \sin \varphi)$ is the in-plane propagating wave vector with φ being an azimuthal angle, and Ω is the frequency of SAWs applied to tWSe₂.

When an inhomogeneous strain is applied to honeycomb lattices, a spatial modulation of the lattice is incorporated into the Hamiltonian as the pseudo-gauge fields [23–36, 43]. Assuming that the tWSe₂ on a piezoelectric substrate completely follows the displacement of the substrate, the Rayleigh-type SAWs-induced pseudo-gauge field reads $\mathbf{A}_s(\mathbf{r}, t) = -\frac{\hbar}{e} \frac{\beta}{2a_0} u_L Q (-\cos 2\varphi, \sin 2\varphi) \text{Im} [e^{i(\mathbf{Q} \cdot \mathbf{r} - \Omega t)}]$, where $\Omega = c_t \xi Q$ and ξ is a constant characterizing the SAWs dispersion [44]. This gives rise to the pseudo-electric field $\mathbf{E}_s(\mathbf{r}, t) = -\partial_t \mathbf{A}_s(\mathbf{r}, t)$ and the pseudo-magnetic field $\mathbf{B}_s(\mathbf{r}, t) = \nabla \times \mathbf{A}_s(\mathbf{r}, t)$, each of which oscillates along a certain direction similarly to linearly-polarized light. Note that the pseudo-gauge fields stemming from the out-

of-plane displacement are proportional to u_z^2 , which are less relevant under weak strain, and hence neglected in the following analysis.

The strain-induced pseudo-gauge field \mathbf{A}_s is coupled to the valley DOF rather than charge DOF, working at the two valley points in the opposite direction: $H_{\tau,l}(\hat{\mathbf{k}}) \rightarrow H_{\tau,l}(\hat{\mathbf{k}} + \frac{e}{\hbar}\tau\mathbf{A}_s(\hat{\mathbf{r}}, t))$ in Eq. (1). Its coupling to the BdG Hamiltonian is given by replacing \hat{H}_τ in Eq. (2) accordingly. To illustrate this, we consider moiré wave-number representation of \hat{H}_{BdG} [41] by assuming a spatially uniform \mathbf{A}_s , for simplicity:

$$H_{\text{BdG}}(\mathbf{k}) = \begin{pmatrix} H_+(\mathbf{k} + \frac{e}{\hbar}\mathbf{A}_s) & \Delta(\mathbf{k}) \\ \Delta^\dagger(\mathbf{k}) & -H_-^T(-\mathbf{k} - \frac{e}{\hbar}\mathbf{A}_s) \end{pmatrix}. \quad (3)$$

This indicates that the pseudo-gauge field couples to the BdG Hamiltonian by $H_{\text{BdG}}(\mathbf{k}) \rightarrow H_{\text{BdG}}(\mathbf{k} + \frac{e}{\hbar}\mathbf{A}_s)$, in the same way as the coupling of electromagnetic gauge fields to Bloch electrons, when the \mathbf{k} dependence of $\Delta(\mathbf{k})$ is not significant [41]. As a result, the quantum geometry of Bogoliubov quasiparticles is relevant to SAW-induced excitations. This observation stands in sharp contrast to and illustrates the advantage of SAWs over optical responses, where the gauge field couples to $H_{\text{BdG}}(\mathbf{k})$ with the opposite signs in the particle and hole sectors reflecting their negative and positive charges, and therefore cannot directly capture the quantum geometry of Bogoliubov quasiparticles in momentum space.

Strictly speaking, the pseudo-gauge field is not the only way that strain affects the system, and there exists correction from the strain-induced coordinate transformations [45], the effective electromagnetic scalar [31] and vector potentials [46, 47], and the vorticity field that behaves as an emergent valley polarization [47]. Notably, the presence of heterostrain component in moiré multilayers induced by SAWs may also trigger nontrivial responses. Here, however, we focus on the homostrain contributions to the pseudo-gauge field as the primary source and leave the investigation of the other effects to future work.

Superconducting acoustogalvanic effect.— The pseudo-electric field \mathbf{E}_s is known to give rise to nonlinear responses in the normal state, referred to as the acoustogalvanic effect (AGE) [27, 31]. In this Letter, we propose its counterpart in the superconducting state, namely the superconducting AGE (SAGE) as a probe of exotic superconductivity in two-dimensional materials. We define the SAGE as the rectification charge current driven by SAWs-induced pseudo-gauge fields:

$$\langle \hat{\mathcal{J}}^\alpha \rangle = \chi_{\mathbf{Q}, -\mathbf{Q}}^{\alpha; \beta\gamma}(0; \Omega, -\Omega) A_s^\beta(\mathbf{Q}, \Omega) A_s^\gamma(-\mathbf{Q}, -\Omega), \quad (4)$$

where $\langle \hat{\mathcal{J}}^\alpha \rangle$ represents the spatio-temporally uniform charge current and $\mathbf{A}_s(\mathbf{Q}, \Omega)$ is a Fourier component of the pseudo-gauge field. Note that the finite momentum transfer \mathbf{Q} should be incorporated, although it is usually neglected for optical responses. This is because Q is

much larger than that for optical responses due to the difference in speed of sound and light. Note also that only (β, γ) -symmetric components contribute among various components of $\chi_{\mathbf{Q}, -\mathbf{Q}}^{\alpha; \beta\gamma}$, since \mathbf{A}_s is linearly polarized. In the following, we concentrate on the propagation directions $\varphi = 0$ and $2\pi/3$ where the pseudo-magnetic field vanishes, and rewrite Eq. (4) in the form of conductivity,

$$\langle \hat{\mathcal{J}}^\alpha \rangle = \sigma_{\mathbf{Q}, -\mathbf{Q}}^{\alpha; \beta\gamma}(0; \Omega, -\Omega) E_s^\beta(\mathbf{Q}, \Omega) E_s^\gamma(-\mathbf{Q}, -\Omega), \quad (5)$$

to highlight the similarity to the optical responses.

Similarly to the nonlinear optical responses [48, 49], the acoustogalvanic conductivity $\sigma_{\mathbf{Q}, -\mathbf{Q}}^{\alpha; \beta\gamma}(0; \Omega, -\Omega)$ is divided into several contributions with different physical origins. In this Letter, we focus on that corresponds to the injection current, which is expected to be dominant in the clean-limit superconductors and therefore relevant to unconventional superconductivity. By generalizing the derivation of nonlinear optical responses [11], this contribution, $\sigma_{\text{inj}}^{\alpha; \beta\gamma}$, is given by

$$\sigma_{\text{inj}}^{\alpha; \beta\gamma} = -\frac{e^2 \pi}{2\hbar\Gamma} \int \frac{d^2 \mathbf{k}}{(2\pi)^2} \sum_{a,b} (\mathcal{J}_{aa}^\alpha - \mathcal{J}_{bb}^\alpha) G_{ab}^{\beta\gamma} F_{ab}(\Omega). \quad (6)$$

Here, the indices a and b specify the eigenstates of \hat{H}_{BdG} with the wave numbers $\mathbf{k} + \mathbf{Q}/2$ and $\mathbf{k} - \mathbf{Q}/2$, respectively, while $E_{ab} = E_a - E_b$, $F_{ab}(\Omega) = [f(E_a) - f(E_b)]\delta(\hbar\Omega - E_{ab})$, and $G_{ab}^{\beta\gamma} = (\hbar/e)^2 (\mathcal{V}_{ab}^\beta \mathcal{V}_{ba}^\gamma + \mathcal{V}_{ab}^\gamma \mathcal{V}_{ba}^\beta)/2E_{ab}^2$, with the eigenvalue E_a and Fermi-Dirac distribution function $f(E) = (e^{E/k_B T} + 1)^{-1}$. The \mathbf{k} integral runs over the MBZ. The scattering rate Γ was introduced by replacing the adiabaticity parameter, following the formulation of the injection-current optical responses [11, 50].

The matrix elements such as \mathcal{J}_{aa}^α and \mathcal{V}_{ab}^β represent those for the charge current operator $\hat{\mathcal{J}}^\alpha$ and its counterpart for the pseudo-gauge field, $\hat{\mathcal{V}}^\beta = \lim_{\mathbf{A}_s \rightarrow 0} (-\partial_{A_s^\beta} \hat{H}_{\text{BdG}})$, namely the valley-current operator. The precise expression of \mathcal{V}_{ab}^β with momentum transfer \mathbf{Q} is available in End Matter [41]. We can replace $\partial_{A_s^\beta}$ with ∂_{k_β} when $\partial_{k_\beta} \Delta(\mathbf{k})$ makes negligible contribution to $G_{ab}^{\beta\gamma}$, and then $G_{ab}^{\beta\gamma}$ for $\mathbf{Q} \rightarrow 0$ coincides with the band-resolved quantum metric of Bogoliubov quasiparticles. This replacement is confirmed to be a good approximation for our model of tWSe₂, while we use the rigorous expression for numerical calculations. In this way, various quantum-geometric quantities beyond the band-resolved quantum metric are expected to also appear in different contributions to SAGE, which will be discussed elsewhere.

We can estimate the magnitude of $\sigma_{\text{inj}}^{\alpha; \beta\gamma}$ by considering a parabolic band and a constant order parameter. We then obtain $\sigma_{\text{inj}}^{\alpha; \beta\gamma} = O(\xi_0^2 Q/\Gamma)$ with the coherence length ξ_0 [41]. Thus, a finite SAGE response is expected regardless of the pairing symmetry, and serves as a versatile

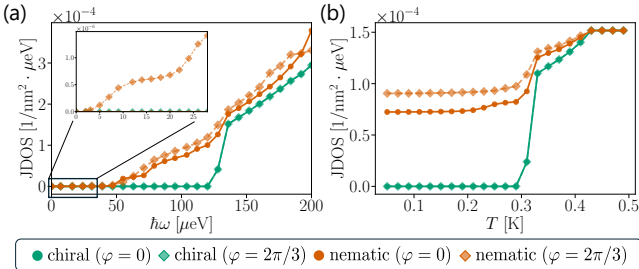


FIG. 3. (a) Frequency and (b) temperature dependencies of JDOS. The green and orange curves correspond to JDOS computed for the chiral and nematic states, respectively, while disks and squares represent $\varphi = 0$ and $\varphi = 2\pi/3$. The results for chiral states with $\varphi = 0$ and $\varphi = 2\pi/3$ coincide as ensured by symmetry.

probe of superconducting states in vdW superconductors. In particular, neither inversion nor time-reversal-symmetry breaking is required due to a finite momentum transfer $\mathbf{Q} \neq 0$, in contrast to the (β, γ) -symmetric optical injection current [11, 48, 49].

Applications to tWSe₂.— We are now ready to investigate the SAGE responses in tWSe₂. In particular, we discuss the frequency and temperature dependences of the acoustogalvanic conductivity Eq. (6). Before evaluating these quantities, we analyze the joint density of states (JDOS), $J_{ab}(\omega; \mathbf{Q}) = \int \frac{d^3 k}{(2\pi)^3} \delta(\hbar\omega - E_a + E_b)$, which quantifies the number of available resonance transitions at a frequency ω between the states a and b with the wave numbers $\mathbf{k} + \mathbf{Q}/2$ and $\mathbf{k} - \mathbf{Q}/2$, respectively. JDOS serves as a qualitative guide to the behavior of the response across different frequencies and temperatures.

The numerical results of JDOS for chiral and nematic superconducting states are shown in Fig. 3. To understand the excitations with a given SAW wave number \mathbf{Q} for $\varphi = 0$ and $2\pi/3$, we first focus on the frequency ω dependence of JDOS at a fixed temperature $T = 50$ mK in Fig. 3(a), which lies well below the critical temperature $T_c = 0.426$ K and thus $\Delta(T) \simeq \Delta_0$. Here and hereafter, we adopt $2\pi/Q = \lambda_{\text{SAW}} \simeq 160$ nm, which corresponds to SAWs with frequency $\Omega/2\pi = 25$ GHz, and thus JDOS at $\hbar\omega = \hbar\Omega \sim 100$ μeV is relevant for the actual responses. Since the superconducting gap is estimated to be $\Delta_0 \simeq 64$ μeV in tWSe₂, the resonance at $\hbar\omega = 2\Delta_0$ is manifested as the typical frequency where JDOS begins to have sizable values. In the chiral state, where a fully-gapped state is realized, JDOS exhibits a vanishing response below the resonance and a sharp peak at $\hbar\omega \simeq 2\Delta_0$. On the other hand, in the nematic state, a finite JDOS persists even below the resonance frequency due to its nodal and anisotropic gap structure. In this case, JDOS depends on the propagation direction φ , as a result of the nematicity.

The temperature dependence of JDOS with a fixed frequency $\hbar\Omega = 100 \mu\text{eV}$ is shown in Fig. 3(b). The JDOS

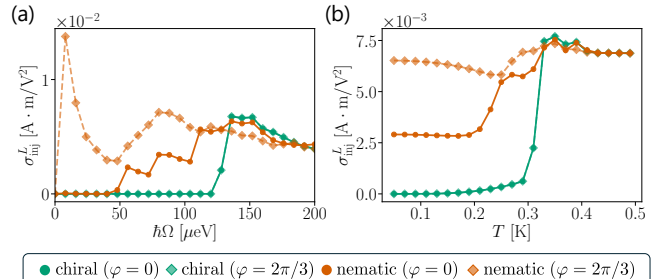


FIG. 4. Frequency (a) and temperature (b) dependencies of the superconducting acoustogalvanic response σ_{inj}^L for chiral and nematic superconducting states. In the chiral state (green line), a strong peak appears when the resonance condition $\hbar\Omega \approx 2\Delta(T)$, is met. In contrast, the nematic state (orange line) exhibits finite responses even when $\hbar\Omega < 2\Delta(T)$ due to the low-energy quasiparticles. We adopt $T = 50$ mK for panel (a) and $\Omega/2\pi = 25$ GHz for panel (b).

remains finite in both the chiral and nematic states as long as the frequency $\hbar\Omega$ is larger than the typical excitation gap $2\Delta(T)$, which grows as temperature is decreased. By further decreasing the temperature, they show significantly different behaviors. In the chiral state, the JDOS rapidly diminishes due to its fully-gapped spectrum. On the other hand, in the nematic state, its nodal and anisotropic gap structure retains a finite JDOS, as low-energy quasiparticles can still resonate.

Based on the insight of JDOS, we discuss the SAGE in $t\text{WSe}_2$. By assuming SAWs directed along $\varphi = 0, 2\pi/3$, \mathbf{Q} and \mathbf{E}_s are parallel, and we then focus on the longitudinal conductivity, $\sigma_{\text{inj}}^L \equiv \hat{Q}_\alpha \sigma_{\text{inj}}^{\alpha;\beta\gamma} \hat{Q}_\beta \hat{Q}_\gamma$, for the chiral and nematic states. This corresponds to $\sigma_{\text{inj}}^{x;xx}$ for $\varphi = 0$, for instance. Figure 4 shows the frequency and temperature dependencies of the acoustogalvanic conductivity σ_{inj}^L for the chiral and nematic states at the same fixed parameters with Fig. 3. We should note that Q is fixed for any frequency Ω of SAWs in Fig. 4(a), to make it easier to compare the results with JDOS in Fig. 3(a). Qualitatively the same results are obtained when frequency-dependent $Q = \Omega/c_t \xi$ is adopted [41].

According to Fig. 4(a), the response of the chiral state is suppressed in the low-frequency regime due to the full-gap structure. As the frequency approaches the resonance frequency $\hbar\Omega = 2\Delta_0$, σ_{inj}^L first shows a resonant peak, as in JDOS. The nematic state exhibits finite responses even at frequencies smaller than $2\Delta_0$ owing to the presence of low-energy quasiparticles. Interestingly, a significant low-frequency enhancement is obtained for $\varphi = 2\pi/3$. As shown in SM, this structure remains even with $\Delta(T) = 0$ (i.e., in the normal state) [41]. This indicates the importance of the resonances near the nodal directions, where the quasiparticles behave similarly to the normal state. Interestingly, the low-frequency enhancement is attributed to the low-frequency divergence

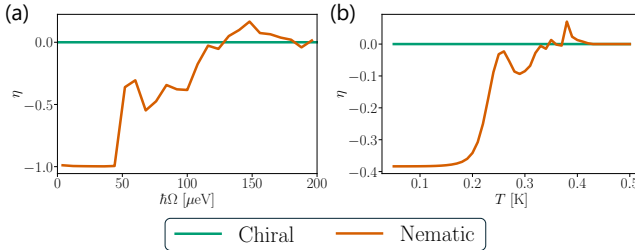


FIG. 5. Frequency (a) and temperature (b) dependencies of the nematicity η for chiral and nematic superconducting states under C_3 rotation. In the chiral state (green line), the C_3 symmetry is preserved, and thus $\eta = 0$. In contrast, the nematic state (orange line) exhibits finite nematicity as a result of spontaneous rotational symmetry breaking.

of the quantum metric with finite momentum transfer $G_{ab}^{\beta\gamma}$ (Eq. (6)) [41], as is understood from the JDOS for $\varphi = 2\pi/3$ lacking the low-frequency divergence. The results illustrate that our SAGE can sensitively probe the low-energy quasiparticles of nodal superconducting states.

The temperature dependence of the acoustogalvanic conductivity in Fig. 4(b) can be understood based on the JDOS (Fig. 3(b)). In the chiral state, a finite response emerges only at temperatures where the resonance condition is satisfied, i.e., when the JDOS becomes non-zero. The response vanishes after $2\Delta(T)$ grows and exceeds Ω . On the other hand, a finite response is always observed below the critical temperature in the nematic state. The different temperature dependence of SAGE will serve as a strong probe of the low-energy excitations, and therefore has the potential to experimentally distinguish the nematic and chiral states.

Furthermore, we investigate the nematicity of the acoustogalvanic conductivity, which is defined by $\eta \equiv \frac{\sigma_{\text{inj}}^L(\varphi=0) - \sigma_{\text{inj}}^L(\varphi=2\pi/3)}{\sigma_{\text{inj}}^L(\varphi=0) + \sigma_{\text{inj}}^L(\varphi=2\pi/3)}$. In the normal and chiral states, the system possesses C_3 rotational symmetry, prohibiting a finite nematicity. In contrast, the spontaneous rotational symmetry breaking in the nematic state allows a finite η , as clearly indicated in Fig. 5: Both the frequency and temperature dependencies demonstrate that only the nematic state exhibits finite nematicity. Therefore, the emergent nematicity below the critical temperature serves as a smoking gun for identifying the pairing symmetry, complementing the information obtained from frequency and temperature dependencies. Thus, our formulation of SAGE opens a new avenue for identifying unconventional superconducting states in vdW materials and beyond.

Discussion.— Finally, we discuss the experimental feasibility of the SAGE. In a realistic experimental condition, the amplitude of charge current is estimated to be of the order of $10 \mu\text{A}/\text{nm}$ with the pseudo-electric field $|\mathbf{E}_s| \simeq 1.5 \times 10^3 \text{ V/m}$ induced by the Rayleigh-

type SAWs, as well as a phenomenological scattering rate $\Gamma = \Delta_0/10$ [41]. Here, we have used the parameters [45, 51, 52]: $u_L \simeq 100 \text{ pm}$, $c_t \simeq 4000 \text{ m/s}$, $\xi \simeq 0.95$, $\beta \sim 2.3$, and $\Omega/2\pi = 25 \text{ GHz}$. The corresponding wavelength $\lambda_{\text{SAW}} \simeq 160 \text{ nm}$ is comparable to the coherence length of tWSe₂ ($\sim 57 \text{ nm}$ [3]), highlighting the significance of the momentum transfer \mathbf{Q} in SAGE. Generally speaking, elastic substrates such as LiNbO₃ also generate a piezoelectric field, inducing the piezoelectric effect [18–20]. This effect can be suppressed by using a non-piezoelectric substrate — such as diamond — with piezoelectric islands and transducers (e.g., AlN) on its surface to generate SAWs [53, 54]. Therefore, we can only investigate the strain-wave-induced phenomena including SAGE.

Most candidates of exotic superconductors exhibit extremely low critical temperatures, typically ranging from 0.1 to 1 K, with superconducting gaps estimated to be on the order of $10^{1-2} \mu\text{eV}$. This energy scale lies outside the accessible range of the conventional optical response. In contrast, SAWs operate in the MHz to GHz range, serving our SAGE as a powerful and suitable tool for probing such low-energy excitations and gap structures. Momentum transfer \mathbf{Q} — ignored in conventional optical responses — is unique to SAWs. This distinction shows that optical response and SAGE probe fundamentally different physics, thereby encoding the value of SAGE as a new experimental probe.

The authors are grateful to R. Hisatomi, Y. Niimi, K. Shinada, H. Tanaka, S. Asano, and Y. Hirobe for fruitful discussions. R.S. thanks Y. Ominato and M. Matsuo for their introduction to the strain gauge fields and SAWs. A. D. thanks Z.-T. Sun for helpful comments on the manuscript. This work was supported by JST SPRING (Grant Number JPMJSP2110) and JSPS KAKENHI (Grants No.JP22KJ1937, No.JP22H01181, No.JP22H04933, No.JP23K17353, No.JP23K22452, No.JP23KK0248, No.JP24H00007, No.JP24H01662, No.JP24K21530, and No.JP25H01249).

* matsumoto.tsugumi.78w@st.kyoto-u.ac.jp

- [1] Y. Cao, V. Fatemi, S. Fang, K. Watanabe, T. Taniguchi, E. Kaxiras, and P. Jarillo-Herrero, Unconventional superconductivity in magic-angle graphene superlattices, *Nature* **556**, 43 (2018).
- [2] Y. Xia, Z. Han, K. Watanabe, T. Taniguchi, J. Shan, and K. F. Mak, Superconductivity in twisted bilayer WSe₂, *Nature* **637**, 833 (2025).
- [3] Y. Guo, J. Pack, J. Swann, L. Holtzman, M. Cothrine, K. Watanabe, T. Taniguchi, D. G. Mandrus, K. Barmak, J. Hone, A. J. Millis, A. Pasupathy, and C. R. Dean, Superconductivity in 5.0° twisted bilayer WSe₂, *Nature* **637**, 839 (2025).
- [4] M. Bélanger, J. Fournier, and D. Sénéchal, Superconductivity in the twisted bilayer transition metal dichalcogenides, *Nature* **637**, 847 (2025).

genide WSe₂ : A quantum cluster study, *Phys. Rev. B.* **106**, 235135 (2022).

[5] Y.-M. Wu, Z. Wu, and H. Yao, Pair-density-wave and chiral superconductivity in twisted bilayer transition metal dichalcogenides, *Phys. Rev. Lett.* **130**, 126001 (2023).

[6] C. Schrade and L. Fu, Nematic, chiral, and topological superconductivity in twisted transition metal dichalcogenides, *Phys. Rev. B.* **110**, 035143 (2024).

[7] D. Guerci, D. Kaplan, J. Ingham, J. H. Pixley, and A. J. Millis, Topological superconductivity from repulsive interactions in twisted WSe₂ (2024), [arXiv:2408.16075 \[cond-mat.supr-con\]](https://arxiv.org/abs/2408.16075).

[8] Y. Tokura and N. Nagaosa, Nonreciprocal responses from non-centrosymmetric quantum materials, *Nat. Commun.* **9**, 3740 (2018).

[9] N. Nagaosa and Y. Yanase, Nonreciprocal transport and optical phenomena in quantum materials, *Annu. Rev. Condens. Matter Phys.* **15**, 63 (2024).

[10] Z. Wang, L. Dong, C. Xiao, and Q. Niu, Berry curvature effects on quasiparticle dynamics in superconductors, *Phys. Rev. Lett.* **126**, 187001 (2021).

[11] H. Watanabe, A. Daido, and Y. Yanase, Nonreciprocal optical response in parity-breaking superconductors, *Phys. Rev. B.* **105**, 024308 (2022).

[12] H. Watanabe, A. Daido, and Y. Yanase, Nonreciprocal meissner response in parity-mixed superconductors, *Phys. Rev. B.* **105**, L100504 (2022).

[13] H. Tanaka, H. Watanabe, and Y. Yanase, Nonlinear optical responses in noncentrosymmetric superconductors, *Phys. Rev. B* **107**, 024513 (2023).

[14] H. Tanaka, H. Watanabe, and Y. Yanase, Nonlinear optical response in superconductors in magnetic field: Quantum geometry and topological superconductivity, *Phys. Rev. B.* **110**, 014520 (2024).

[15] H. Tanaka and Y. Yanase, Vertex correction for the linear and nonlinear optical responses in superconductors: Multiband effect and topological superconductivity, *Phys. Rev. B.* **112**, 094503 (2025).

[16] O. Matsyshyn, G. Vignale, and J. C. W. Song, Superconducting berry curvature dipole (2024), [arXiv:2410.21363 \[cond-mat.supr-con\]](https://arxiv.org/abs/2410.21363).

[17] D. Kaplan, K. P. Lucht, P. A. Volkov, and J. H. Pixley, Quantum geometric photocurrents of quasiparticles in superconductors (2025), [arXiv:2502.12265 \[cond-mat.supr-con\]](https://arxiv.org/abs/2502.12265).

[18] V. I. Fal'ko, VI, S. V. Meshkov, and S. V. Iordanskii, Acoustoelectric drag effect in the two-dimensional electron gas at strong magnetic field, *Phys. Rev. B* **47**, 9910 (1993).

[19] V. Miseikis, J. E. Cunningham, K. Saeed, R. O'Rourke, and A. G. Davies, Acoustically induced current flow in graphene, *Appl. Phys. Lett.* **100**, 133105 (2012).

[20] L. Bandhu, L. M. Lawton, and G. R. Nash, Macroscopic acoustoelectric charge transport in graphene, *Appl. Phys. Lett.* **103**, 133101 (2013).

[21] K. Sonowal, A. V. Kalameitsev, V. M. Kovalev, and I. G. Savenko, Acoustoelectric effect in two-dimensional dirac materials exposed to rayleigh surface acoustic waves, *Phys. Rev. B.* **102**, 235405 (2020).

[22] Y. Mou, J. Wang, H. Chen, Y. Xia, H. Li, Q. Yan, X. Jiang, Y. Wu, W. Shi, H. Jiang, X. C. Xie, and C. Zhang, Coherent detection of the oscillating acoustoelectric effect in graphene, *Phys. Rev. Lett.* **134**, 096301 (2025).

[23] F. von Oppen, F. Guinea, and E. Mariani, Synthetic electric fields and phonon damping in carbon nanotubes and graphene, *Phys. Rev. B* **80**, 075420 (2009).

[24] A. Vaezi, N. Abedpour, R. Asgari, A. Cortijo, and M. A. H. Vozmediano, Topological electric current from time-dependent elastic deformations in graphene, *Phys. Rev. B* **88**, 125406 (2013).

[25] M. A. Cazalilla, H. Ochoa, and F. Guinea, Quantum spin hall effect in two-dimensional crystals of transition-metal dichalcogenides, *Phys. Rev. Lett.* **113**, 077201 (2014).

[26] A. V. Kalameitsev, V. M. Kovalev, and I. G. Savenko, Valley acoustoelectric effect, *Phys. Rev. Lett.* **122**, 256801 (2019).

[27] P. O. Sukhachov and H. Rostami, Acoustogalvanic effect in dirac and weyl semimetals, *Phys. Rev. Lett.* **124**, 126602 (2020).

[28] E. Sela, Y. Bloch, F. von Oppen, and M. B. Shalom, Quantum hall response to time-dependent strain gradients in graphene, *Phys. Rev. Lett.* **124**, 026602 (2020).

[29] S.-Y. Li, Y. Su, Y.-N. Ren, and L. He, Valley polarization and inversion in strained graphene via pseudo-landau levels, valley splitting of real landau levels, and confined states, *Phys. Rev. Lett.* **124**, 106802 (2020).

[30] P. Zhao, C. H. Sharma, R. Liang, C. Glaserapp, L. Mourokh, V. M. Kovalev, P. Huber, M. Prada, L. Tieemann, and R. H. Blick, Acoustically induced giant synthetic hall voltages in graphene, *Phys. Rev. Lett.* **128**, 256601 (2022).

[31] P. Bhalla, G. Vignale, and H. Rostami, Pseudogauge field driven acoustoelectric current in two-dimensional hexagonal dirac materials, *Phys. Rev. B* **105**, 125407 (2022).

[32] B. Uchoa and Y. Barlas, Superconducting states in pseudo-landau-levels of strained graphene, *Phys. Rev. Lett.* **111**, 046604 (2013).

[33] G. Massarelli, G. Wachtel, J. Y. T. Wei, and A. Paramkanti, Pseudo-landau levels of bogoliubov quasiparticles in strained nodal superconductors, *Phys. Rev. B* **96**, 224516 (2017).

[34] E. M. Nica and M. Franz, Landau levels from neutral bogoliubov particles in two-dimensional nodal superconductors under strain and doping gradients, *Phys. Rev. B* **97**, 024520 (2018).

[35] M. M. Nayga, S. Rachel, and M. Vojta, Magnon landau levels and emergent supersymmetry in strained antiferromagnets, *Phys. Rev. Lett.* **123**, 207204 (2019).

[36] R. Sano, Y. Ominato, and M. Matsuo, Acustomagnonic spin hall effect in honeycomb antiferromagnets, *Phys. Rev. Lett.* **132**, 236302 (2024).

[37] Y. Yamazaki, T. Funato, and A. Yamakage, Majorana spin current generation by dynamic strain, *Phys. Rev. B.* **108**, L060505 (2023).

[38] F. Wu, T. Lovorn, E. Tutuc, I. Martin, and A. H. MacDonald, Topological insulators in twisted transition metal dichalcogenide homobilayers, *Phys. Rev. Lett.* **122**, 086402 (2019).

[39] T. Devakul, V. Crépel, Y. Zhang, and L. Fu, Magic in twisted transition metal dichalcogenide bilayers, *Nat. Commun.* **12**, 6730 (2021).

[40] J. Zhu, Y.-Z. Chou, M. Xie, and S. Das Sarma, Superconductivity in twisted transition metal dichalcogenide homobilayers, *Phys. Rev. B* **111**, L060501 (2025).

[41] See Supplemental Material for more details.

[42] X. Nie, X. Wu, Y. Wang, S. Ban, Z. Lei, J. Yi, Y. Liu, and Y. Liu, Surface acoustic wave induced phenomena in two-

dimensional materials, *Nanoscale Horiz* **8**, 158 (2023).

[43] J.-X. Hu, C.-P. Zhang, Y.-M. Xie, and K. T. Law, Non-linear hall effects in strained twisted bilayer WSe₂, *Commun. Phys.* **5**, 1 (2022).

[44] L. D. Landau, E. M. Lifshitz, A. M. Kosevich, and L. P. Pitaevskii, *Theory of elasticity: volume 7*, Course of theoretical physics (Elsevier Science, Kidlington, England, 1986).

[45] Z. Bi, N. F. Q. Yuan, and L. Fu, Designing flat bands by strain, *Phys. Rev. B* **100**, 035448 (2019).

[46] M. Koshino and T. Ando, Anomalous orbital magnetism in dirac-electron systems: Role of pseudospin paramagnetism, *Phys. Rev. B* **81**, 195431 (2010).

[47] Y. Ominato, D. Oue, and M. Matsuo, Valley transport driven by dynamic lattice distortion, *Phys. Rev. B* **105**, 195409 (2022).

[48] J. Ahn, G.-Y. Guo, and N. Nagaosa, Low-frequency divergence and quantum geometry of the bulk photovoltaic effect in topological semimetals, *Phys. Rev. X* **10**, 041041 (2020).

[49] H. Watanabe and Y. Yanase, Chiral photocurrent in parity-violating magnet and enhanced response in topo-logical antiferromagnet, *Phys. Rev. X* **11**, 011001 (2021).

[50] See End Matter for more details.

[51] S. Fang, S. Carr, M. A. Cazalilla, and E. Kaxiras, Electronic structure theory of strained two-dimensional materials with hexagonal symmetry, *Phys. Rev. B* **98**, 075106 (2018).

[52] A. A. Maznev, R. Mincigrucci, F. Bencivenga, V. Unikandanunni, F. Capotondi, G. Chen, Z. Ding, R. A. Duncan, L. Foglia, M. G. Izzo, C. Masciovecchio, A. Martinelli, G. Monaco, E. Pedersoli, S. Bonetti, and K. A. Nelson, Generation and detection of 50 GHz surface acoustic waves by extreme ultraviolet pulses, *Appl. Phys. Lett.* **119**, 044102 (2021).

[53] F. Bénédic, M. B. Assouar, F. Mohasseb, O. Elmazria, P. Alnot, and A. Gicquel, Surface acoustic wave devices based on nanocrystalline diamond and aluminium nitride, *Diam. Relat. Mater.* **13**, 347 (2004).

[54] J. G. Rodriguez-Madrid, G. F. Iriarte, J. Pedros, O. A. Williams, D. Brink, and F. Calle, Super-high-frequency SAW resonators on AlN/diamond, *IEEE Electron Device Lett.* **33**, 495 (2012).

End Matter

Formulation of SAGE.— Here, we discuss the derivation of the formulas of acoustogalvanic susceptibility.

In the presence of pseudo-gauge field, the normal-state Hamiltonian of the valley τ is written as

$$\hat{H}_\tau[\mathbf{A}_s] = \hat{H}_{\tau,l}[0] - \int \frac{d^2q}{(2\pi)^2} \hat{\mathcal{V}}_\tau^{(\beta,\mathbf{q})} A_s^\beta(\mathbf{q},t) + \frac{1}{2} \int \frac{d^2q}{(2\pi)^2} \int \frac{d^2q'}{(2\pi)^2} \hat{\mathcal{V}}_\tau^{(\beta,\mathbf{q})(\gamma,\mathbf{q}')} A_s^\beta(\mathbf{q},t) A_s^\gamma(\mathbf{q}',t) + O(A_s^3), \quad (7)$$

by using the Fourier coefficients of the pseudo-gauge field,

$$\begin{aligned} \mathbf{A}_s(\mathbf{r},t) &= \int \frac{d^2q}{(2\pi)^2} e^{i\mathbf{q}\cdot\mathbf{r}} \mathbf{A}_s(\mathbf{q},t) \\ &= \int \frac{d^2q}{(2\pi)^2} \int \frac{d\omega}{2\pi} e^{i\mathbf{q}\cdot\mathbf{r}-i\omega t} \mathbf{A}_s(\mathbf{q},\omega). \end{aligned} \quad (8)$$

Here, the current operators for the pseudo-gauge field is given by $\hat{\mathcal{V}}_\tau^{(\beta,\mathbf{q})} = \text{diag}(\hat{\mathcal{V}}_{\tau,b}^{(\beta,\mathbf{q})}, \hat{\mathcal{V}}_{\tau,t}^{(\beta,\mathbf{q})})$ and $\hat{\mathcal{V}}_\tau^{(\beta,\mathbf{q})(\gamma,\mathbf{q}')} =$

$\text{diag}(\hat{\mathcal{V}}_{\tau,b}^{(\beta,\mathbf{q})(\gamma,\mathbf{q}')}, \hat{\mathcal{V}}_{\tau,t}^{(\beta,\mathbf{q})(\gamma,\mathbf{q}')})$, with

$$\hat{\mathcal{V}}_{\tau,l}^{(\beta,\mathbf{q})} = \frac{1}{2} \left\{ \frac{e\hbar\tau}{m^*} (\hat{\mathbf{k}} - \boldsymbol{\kappa}_{\tau,l}), e^{i\mathbf{q}\cdot\hat{\mathbf{r}}} \right\}, \quad (9)$$

$$\hat{\mathcal{V}}_{\tau,l}^{(\beta,\mathbf{q})(\gamma,\mathbf{q}')} = -\frac{e^2\tau^2}{m^*} e^{i(\mathbf{q}+\mathbf{q}')\cdot\hat{\mathbf{r}}} \delta_{\beta\gamma}. \quad (10)$$

Similar expansion is obtained for the BdG Hamiltonian:

$$\hat{H}_{\text{BdG}}[\mathbf{A}_s] = \hat{H}_{\text{BdG}}[0] - \int \frac{d^2q}{(2\pi)^2} \hat{\mathcal{V}}^{(\beta,\mathbf{q})} A_s^\beta(\mathbf{q},t) + \frac{1}{2} \int \frac{d^2q}{(2\pi)^2} \int \frac{d^2q'}{(2\pi)^2} \hat{\mathcal{V}}^{(\beta,\mathbf{q})(\gamma,\mathbf{q}')} A_s^\beta(\mathbf{q},t) A_s^\gamma(\mathbf{q}',t) + O(A_s^3), \quad (11)$$

with $\hat{\mathcal{V}}^{(\beta,\mathbf{q})} = \text{diag}(\hat{\mathcal{V}}_+^{(\beta,\mathbf{q})}, -[\hat{\mathcal{V}}_-^{(\beta,\mathbf{q})}]^T)$, and $\hat{\mathcal{V}}^{(\beta,\mathbf{q})(\gamma,\mathbf{q}')} = \text{diag}(\hat{\mathcal{V}}_+^{(\beta,\mathbf{q})(\gamma,\mathbf{q}')}, \hat{\mathcal{V}}_-^{(\beta,\mathbf{q})(\gamma,\mathbf{q}')})$. For later use, we define

$$\hat{\mathcal{V}}^\beta \equiv \hat{\mathcal{V}}^\beta(\mathbf{q}=0), \quad \hat{\mathcal{V}}^{(\beta,\mathbf{q})} = \frac{1}{2} \left\{ \hat{\mathcal{V}}^\beta, e^{i\mathbf{q}\cdot\hat{\mathbf{r}}} \right\}. \quad (12)$$

It should be noted that $\hat{\mathcal{V}}^\beta = -\lim_{A_s \rightarrow 0} \partial_{A_s^\beta} \hat{H}_{\text{BdG}}(\mathbf{A}_s)$ is

satisfied, where $\hat{H}_{\text{BdG}}(\mathbf{A}_s)$ represents \hat{H}_{BdG} in the presence of spatially uniform pseudo-gauge field.

The acoustogalvanic susceptibility can be derived by solving the von-Neumann equation for the density matrix with the perturbation $\mathbf{A}_s(\mathbf{r},t)$, in the same way as the nonlinear optical responses. For this purpose, it is convenient to rewrite Eq. (11) in the following form by

generalizing the Einstein summation rule:

$$\hat{H}_{\text{BdG}}[\mathbf{A}_s] = \hat{H}_{\text{BdG}} - \hat{\mathcal{V}}^{\bar{\beta}} A_s^{\bar{\beta}}(t) + \frac{1}{2} \hat{\mathcal{V}}^{\bar{\beta}\bar{\gamma}} A_s^{\bar{\beta}}(t) A_s^{\bar{\gamma}}(t) + O(A_s^3). \quad (13)$$

Here, $\bar{\beta} = (\beta, \mathbf{q})$ and

$$\hat{\mathcal{V}}^{\bar{\beta}} A_s^{\bar{\beta}}(t) \equiv \sum_{\beta} \int \frac{d^2 q}{(2\pi)^2} \hat{\mathcal{V}}^{(\beta, \mathbf{q})} A_s^{\beta}(\mathbf{q}, t), \quad (14)$$

for example. By using this notation, we can immediately obtain the acoustogalvanic susceptibility based on the results of the optical conductivity [11]. This is achieved by replacing the gauge-field derivative $\partial_{A^{\beta}}$ and $\partial_{A^{\gamma}}$ with the pseudo-gauge-field derivative $\partial_{A_s^{\bar{\beta}}}$ and $\partial_{A_s^{\bar{\gamma}}}$. Thus, the acoustogalvanic susceptibility corresponding to the injection-current optical response is given by

$$\sigma_{\mathbf{Q}, -\mathbf{Q}}^{\alpha; \beta\gamma}(0; \Omega, -\Omega) = \sigma^{\alpha; \bar{\beta}, \bar{\gamma}}(0; \Omega, -\Omega) = -\frac{\hbar\pi}{2\eta} \frac{1}{(\hbar\Omega)^2} \frac{1}{S} \sum_{a,b} \delta \mathcal{J}_{ab}^{\alpha} \mathcal{V}_{ab}^{\bar{\beta}} \mathcal{V}_{ba}^{\bar{\gamma}} f_{ab} \delta(\hbar\Omega - E_{ab}), \quad (15)$$

with $\bar{\beta} = (\beta, \mathbf{Q})$, $\bar{\gamma} = (\gamma, -\mathbf{Q})$, and the system area S . The removal of the overall coefficient $1/2$ from the expression in Ref. [11] is due to the different conventions of the BdG Hamiltonian: That in Ref. [11] has a twice larger matrix size than that in this paper. In this expression, the indices a and b independently run over all the eigenstates of \hat{H}_{BdG} including both the band-index and wave-

number DOFs. The quantities in the summand are defined by $\mathcal{V}_{ab}^{\bar{\beta}} \equiv \langle \psi_a | \hat{\mathcal{V}}^{\bar{\beta}} | \psi_b \rangle$ with $\hat{H}_{\text{BdG}} |\psi_a\rangle = E_a |\psi_a\rangle$, as well as $\delta \mathcal{J}_{ab}^{\alpha} = \mathcal{J}_{aa}^{\alpha} - \mathcal{J}_{bb}^{\alpha}$ with $\mathcal{J}_{aa}^{\alpha} = \langle \psi_a | \hat{\mathcal{J}}^{\alpha} | \psi_a \rangle$. We defined the spatially-uniform charge current operator $\hat{\mathcal{J}}^{\alpha}$ by the gauge-field derivative of the BdG Hamiltonian [11]. In particular, we can write $\hat{\mathcal{J}}^{\alpha} = \hat{\mathcal{V}}^{\beta} \tau_z$ for the case of Eq. (3), with the Pauli matrix τ_z in the Nambu space.

Let us redefine a and b to represent the band indices of the BdG Hamiltonian, and $a \rightarrow (\mathbf{k}_a, a)$ and $b \rightarrow (\mathbf{k}_b, b)$. Then, the matrix element $\mathcal{V}_{ab}^{\bar{\beta}}$ reduces to

$$\mathcal{V}_{ab}^{\bar{\beta}} = \langle \psi_a(\mathbf{k}_a) | \hat{\mathcal{V}}^{(\beta, \mathbf{Q})} | \psi_b(\mathbf{k}_b) \rangle = \delta_{\mathbf{k}_a, \mathbf{k}_b + \mathbf{Q}} \mathcal{V}_{ab}(\mathbf{k}_a, \mathbf{k}_b), \quad (16)$$

with

$$\mathcal{V}_{ab}^{\beta}(\mathbf{k}_a, \mathbf{k}_b) \equiv \left\langle u_a(\mathbf{k}_a) \left| \frac{\hat{\mathcal{V}}^{\beta}(\mathbf{k}_a) + \hat{\mathcal{V}}^{\beta}(\mathbf{k}_b)}{2} \right| u_b(\mathbf{k}_b) \right\rangle. \quad (17)$$

We defined $\hat{\mathcal{V}}^{\beta}(\mathbf{k}) = e^{-i\mathbf{k}\cdot\hat{\mathbf{r}}} \hat{\mathcal{V}}^{\beta} e^{i\mathbf{k}\cdot\hat{\mathbf{r}}}$ and denoted the Bloch state for the BdG Hamiltonian by $|\psi_a(\mathbf{k})\rangle = e^{i\mathbf{k}\cdot\hat{\mathbf{r}}} |u_a(\mathbf{k})\rangle$ with its periodic part $|u_a(\mathbf{k})\rangle$. By defining

$$\mathcal{J}_{aa}^{\alpha}(\mathbf{k}_a) \equiv \langle u_a(\mathbf{k}_a) | \hat{\mathcal{J}}^{\alpha}(\mathbf{k}_a) | u_a(\mathbf{k}_a) \rangle, \quad (18)$$

$$\hat{\mathcal{J}}^{\alpha}(\mathbf{k}_a) = e^{-i\mathbf{k}_a \cdot \hat{\mathbf{r}}} \mathcal{J}^{\alpha} e^{i\mathbf{k}_a \cdot \hat{\mathbf{r}}}, \quad (19)$$

and introducing $\mathbf{k}_a = \mathbf{k} + \mathbf{Q}/2$, we obtain

$$\begin{aligned} \sigma_{\text{inj}}^{\alpha; \beta\gamma} &= \frac{\sigma^{\alpha; \bar{\beta}, \bar{\gamma}}(0; \Omega, -\Omega) + (\beta \leftrightarrow \gamma)}{2} \\ &= -\frac{1}{2} \frac{\hbar\pi}{2\eta} \frac{1}{S} \sum_{\mathbf{k}, \mathbf{k}_a, \mathbf{k}_b, a, b} \delta_{\mathbf{k}_a, \mathbf{k} + \frac{\mathbf{Q}}{2}} \delta_{\mathbf{k}_b, \mathbf{k} - \frac{\mathbf{Q}}{2}} (\mathcal{J}_{aa}^{\alpha}(\mathbf{k}_a) - \mathcal{J}_{bb}^{\alpha}(\mathbf{k}_b)) \frac{\mathcal{V}_{ab}^{\beta}(\mathbf{k}_a, \mathbf{k}_b) \mathcal{V}_{ba}^{\gamma}(\mathbf{k}_b, \mathbf{k}_a)}{(E_a(\mathbf{k}_a) - E_b(\mathbf{k}_b))^2} \\ &\quad \times \left[f(E_a(\mathbf{k}_a)) - f(E_b(\mathbf{k}_b)) \right] \delta(\hbar\Omega - E_a(\mathbf{k}_a) + E_b(\mathbf{k}_b)) + (\beta \leftrightarrow \gamma). \end{aligned} \quad (20)$$

By replacing $(1/S) \sum_{\mathbf{k}}$ with $\int \frac{d^2 k}{(2\pi)^2}$, we obtain the formula in the main text. For numerical calculations, we use the moiré wave-number representation of the BdG Hamiltonian to evaluate its eigenstates and eigenvalues, as well as the current operators corresponding to the gauge and pseudo-gauge fields. For example, $\mathcal{V}^{\beta}(\mathbf{k})$ can be obtained by $-\lim_{A_s \rightarrow 0} \partial_{A_s^{\beta}} H_{\text{BdG}}(\mathbf{k}, \mathbf{A}_s)$ with $H_{\text{BdG}}(\mathbf{k}, \mathbf{A}_s)$ given in Eq. (3).

Supplemental Material for Superconducting Acoustogalvanic Effect in Twisted Transition Metal Dichalcogenides

Tsugumi Matsumoto,^{1,*} Ryotaro Sano,^{1,2} Youichi Yanase,¹ and Akito Daido^{1,3}

¹*Department of Physics, Graduate School of Science, Kyoto University, Kyoto 606-8502, Japan*

²*Institute of Solid State Physics, University of Tokyo, Kashiwa 277-8581, Japan*

³*Department of Physics, Hong Kong University of Science and Technology, Clear Water Bay, Hong Kong, China*

Moiré wave-number representation of the continuum model

In this section, we introduce the moiré wave-number representation of the continuum model. The original continuum model [1] is given by

$$H_\tau = \int d\mathbf{r} \Psi_\tau^\dagger(\mathbf{r}) \begin{pmatrix} \hat{H}_{\tau,b}(\hat{\mathbf{k}}) + \Delta_b(\mathbf{r}) & T_\tau(\mathbf{r}) \\ T_\tau^\dagger(\mathbf{r}) & \hat{H}_{\tau,t}(\hat{\mathbf{k}}) + \Delta_t(\mathbf{r}) \end{pmatrix} \Psi_\tau(\mathbf{r}), \quad (\text{S.1})$$

where the components are given by

$$\hat{H}_{\tau,l}(\hat{\mathbf{k}}) = -\frac{\hbar^2}{2m^*}(\hat{\mathbf{k}} - \boldsymbol{\kappa}_{\tau,l})^2 - l\frac{V_z}{2}, \quad (\text{S.2})$$

$$\Delta_l(\mathbf{r}) = V \sum_{j=1,2,3} e^{i(\mathbf{g}_j \cdot \mathbf{r} + l\psi)} + \text{h.c.}, \quad (\text{S.3})$$

$$T_\tau(\mathbf{r}) = w(1 + e^{+i\tau\mathbf{g}_2 \cdot \mathbf{r}} + e^{-i\tau\mathbf{g}_3 \cdot \mathbf{r}}). \quad (\text{S.4})$$

We define the Fourier transformation of the field operator by

$$\psi_l^\dagger(\mathbf{r}) = \int_{-\infty}^{\infty} \frac{d\mathbf{k}}{\sqrt{(2\pi)^2}} e^{-i\mathbf{k} \cdot \mathbf{r}} c_l^\dagger(\mathbf{k}), \quad (\text{S.5})$$

and obtain

$$\begin{aligned} H_m^\tau &= \int d\mathbf{r} \psi_l^\dagger(\mathbf{r}) \hat{H}_{\tau,l}(-i\boldsymbol{\nabla}) \psi_l(\mathbf{r}) \\ &= \int_{-\infty}^{\infty} \frac{d\mathbf{k}}{(2\pi)^2} c_l^\dagger(\mathbf{k}) H_{\tau,l}(\mathbf{k}) c_l(\mathbf{k}), \end{aligned} \quad (\text{S.6})$$

$$\begin{aligned} H_\Delta^\tau &= \int d\mathbf{r} \psi_l^\dagger(\mathbf{r}) \Delta_l(\mathbf{r}) \psi_l(\mathbf{r}) \\ &= V e^{il\psi} \sum_{j=1,2,3} \int d\mathbf{r} \psi_l^\dagger(\mathbf{r}) e^{i\mathbf{g}_j \cdot \mathbf{r}} \psi_l(\mathbf{r}) + \text{h.c.} \\ &= \int_{-\infty}^{\infty} \frac{d\mathbf{k}}{(2\pi)^2} V \sum_j \left[e^{+il\psi} c_l^\dagger(\mathbf{k} + \mathbf{g}_j) c_l(\mathbf{k}) + e^{-il\psi} c_l^\dagger(\mathbf{k}) c_l(\mathbf{k} + \mathbf{g}_j) \right], \end{aligned} \quad (\text{S.7})$$

$$\begin{aligned} H_T^\tau &= \int d\mathbf{r} \psi_b^\dagger(\mathbf{r}) T_\tau(\mathbf{r}) \psi_t(\mathbf{r}) + \text{h.c.} \\ &= \int d\mathbf{r} \psi_b^\dagger(\mathbf{r}) w(1 + e^{-i\tau\mathbf{g}_2 \cdot \mathbf{r}} + e^{+i\tau\mathbf{g}_3 \cdot \mathbf{r}}) \psi_t(\mathbf{r}) + \text{h.c.} \\ &= w \int_{-\infty}^{\infty} \frac{d\mathbf{k}}{(2\pi)^2} \left[c_b^\dagger(\mathbf{k}) c_t(\mathbf{k}) + c_b^\dagger(\mathbf{k}) c_t(\mathbf{k} - \tau\mathbf{g}_2) + c_b^\dagger(\mathbf{k} - \tau\mathbf{g}_3) c_t(\mathbf{k}) \right] + \text{h.c.}, \end{aligned} \quad (\text{S.8})$$

where $\mathbf{g}_j = \frac{4\pi}{\sqrt{3}L_M} \left(\cos \frac{2(j-1)\pi}{3}, \sin \frac{2(j-1)\pi}{3} \right)$ represents moiré reciprocal lattice vectors. In this work, we only consider the first-order interlayer coupling and hence, we choose the basis as

$$\Psi_b(\mathbf{k}) = (c_b(\mathbf{k}), c_b(\mathbf{k} + \mathbf{g}_1), c_b(\mathbf{k} - \mathbf{g}_3)), \quad (\text{S.9})$$

$$\Psi_t(\mathbf{k}) = (c_t(\mathbf{k}), c_t(\mathbf{k} + \mathbf{g}_1), c_t(\mathbf{k} - \mathbf{g}_2)), \quad (\text{S.10})$$

by keeping the states near the original massive Dirac cones of the bottom and top layers, respectively. Here, \mathbf{k} represents the wave number in the moiré Brillouin zone (MBZ). In the following discussion, we focus on the valley $\tau = +$. By rewriting H_m as

$$H_m^+ = \int_{-\infty}^{\infty} \frac{d\mathbf{k}}{(2\pi)^2} c_l^\dagger(\mathbf{k}) H_l(\mathbf{k}) c_l(\mathbf{k}) \quad (\text{S.11})$$

$$= \sum_{n,m \in \mathbb{Z}} \int_{\text{MBZ}} \frac{d\mathbf{k}}{(2\pi)^2} c_l^\dagger(\mathbf{k} + n\mathbf{g}_1 + m\mathbf{g}_2) H_l(\mathbf{k} + n\mathbf{g}_1 + m\mathbf{g}_2) c_l(\mathbf{k} + n\mathbf{g}_1 + m\mathbf{g}_2), \quad (\text{S.12})$$

and keeping the states specified by $\Psi_b(\mathbf{k})$ and $\Psi_t(\mathbf{k})$, we obtain $H_m^+ = H_m^b + H_m^t$ with

$$H_m^b = \int_{\text{MBZ}} \frac{d\mathbf{k}}{(2\pi)^2} \Psi_b^\dagger(\mathbf{k}) \begin{pmatrix} H_b(\mathbf{k}) & 0 & 0 \\ 0 & H_b(\mathbf{k} + \mathbf{g}_1) & 0 \\ 0 & 0 & H_b(\mathbf{k} - \mathbf{g}_3) \end{pmatrix} \Psi_b(\mathbf{k}) \equiv \int_{\text{MBZ}} \frac{d\mathbf{k}}{(2\pi)^2} \Psi_b^\dagger(\mathbf{k}) h_m^b(\mathbf{k}) \Psi_b(\mathbf{k}), \quad (\text{S.13})$$

$$H_m^t = \int_{\text{MBZ}} \frac{d\mathbf{k}}{(2\pi)^2} \Psi_t^\dagger(\mathbf{k}) \begin{pmatrix} H_t(\mathbf{k}) & 0 & 0 \\ 0 & H_t(\mathbf{k} + \mathbf{g}_1) & 0 \\ 0 & 0 & H_t(\mathbf{k} - \mathbf{g}_2) \end{pmatrix} \Psi_t(\mathbf{k}) \equiv \int_{\text{MBZ}} \frac{d\mathbf{k}}{(2\pi)^2} \Psi_t^\dagger(\mathbf{k}) h_m^t(\mathbf{k}) \Psi_t(\mathbf{k}). \quad (\text{S.14})$$

Here and hereafter in this Supplemental Material, we represent the integral over the MBZ by $\int_{\text{MBZ}} \frac{d\mathbf{k}}{(2\pi)^2}$ to emphasize the difference from $\int_{-\infty}^{\infty} \frac{d\mathbf{k}}{(2\pi)^2}$, instead of $\int \frac{d\mathbf{k}}{(2\pi)^2}$ adopted in the main text. To rewrite $H_\Delta(j)$ and $H_T(j)$, we introduce the decomposition

$$H_\Delta = \sum_j H_\Delta(j), \quad (\text{S.15})$$

$$H_T = \sum_j H_T(j), \quad (\text{S.16})$$

and then, each components are given by

$$\begin{aligned} H_\Delta(1) &= \int_{-\infty}^{\infty} \frac{d\mathbf{k}}{(2\pi)^2} V e^{+il\psi} c_l^\dagger(\mathbf{k} + \mathbf{g}_1) c_l(\mathbf{k}) + \text{h.c.} \\ &= \int_{\text{MBZ}} \frac{d\mathbf{k}}{(2\pi)^2} V e^{+il\psi} c_l^\dagger(\mathbf{k} + \mathbf{g}_1) c_l(\mathbf{k}) + \text{h.c.} + (\text{other } \mathbf{k}), \end{aligned} \quad (\text{S.17})$$

$$\begin{aligned} H_\Delta(2) &= \int_{-\infty}^{\infty} \frac{d\mathbf{k}}{(2\pi)^2} V e^{+il\psi} c_l^\dagger(\mathbf{k} + \mathbf{g}_2) c_l(\mathbf{k}) + \text{h.c.} \\ &= \int_{-\infty}^{\infty} \frac{d\mathbf{k}}{(2\pi)^2} V e^{+il\psi} c_l^\dagger(\mathbf{k}) c_l(\mathbf{k} - \mathbf{g}_2) + \text{h.c.} \\ &= \int_{\text{MBZ}} \frac{d\mathbf{k}}{(2\pi)^2} V e^{+il\psi} \left[c_l^\dagger(\mathbf{k}) c_l(\mathbf{k} - \mathbf{g}_2) + c_l^\dagger(\mathbf{k} - \mathbf{g}_3) c_l(\mathbf{k} + \mathbf{g}_1) \right] + \text{h.c.} + (\text{other } \mathbf{k}), \end{aligned} \quad (\text{S.18})$$

$$\begin{aligned} H_\Delta(3) &= \int_{-\infty}^{\infty} \frac{d\mathbf{k}}{(2\pi)^2} V e^{+il\psi} c_l^\dagger(\mathbf{k} + \mathbf{g}_3) c_l(\mathbf{k}) + \text{h.c.} \\ &= \int_{-\infty}^{\infty} \frac{d\mathbf{k}}{(2\pi)^2} V e^{+il\psi} c_l^\dagger(\mathbf{k}) c_l(\mathbf{k} - \mathbf{g}_3) + \text{h.c.} \\ &= \int_{\text{MBZ}} \frac{d\mathbf{k}}{(2\pi)^2} V e^{+il\psi} \left[c_l^\dagger(\mathbf{k}) c_l(\mathbf{k} - \mathbf{g}_3) + c_l^\dagger(\mathbf{k} - \mathbf{g}_2) c_l(\mathbf{k} + \mathbf{g}_1) \right] + \text{h.c.} + (\text{other } \mathbf{k}), \end{aligned} \quad (\text{S.19})$$

and

$$\begin{aligned}
H_T(1) &= \int_{-\infty}^{\infty} \frac{d\mathbf{k}}{(2\pi)^2} w c_b^\dagger(\mathbf{k}) c_t(\mathbf{k}) + \text{h.c.} \\
&= \int_{\text{MBZ}} \frac{d\mathbf{k}}{(2\pi)^2} w \left[c_b^\dagger(\mathbf{k}) c_t(\mathbf{k}) + c_b^\dagger(\mathbf{k} + \mathbf{g}_1) c_t(\mathbf{k} + \mathbf{g}_1) \right. \\
&\quad \left. + c_b^\dagger(\mathbf{k} - \mathbf{g}_3) c_t(\mathbf{k} - \mathbf{g}_3) + c_b^\dagger(\mathbf{k} - \mathbf{g}_2) c_t(\mathbf{k} - \mathbf{g}_2) \right] + \text{h.c.} + (\text{other } \mathbf{k}),
\end{aligned} \tag{S.20}$$

$$\begin{aligned}
H_T(2) &= \int_{-\infty}^{\infty} \frac{d\mathbf{k}}{(2\pi)^2} w c_b^\dagger(\mathbf{k} + \mathbf{g}_2) c_t(\mathbf{k}) + \text{h.c.} \\
&= \int_{\text{MBZ}} \frac{d\mathbf{k}}{(2\pi)^2} w \left[c_b^\dagger(\mathbf{k}) c_t(\mathbf{k} - \mathbf{g}_2) + c_b^\dagger(\mathbf{k} - \mathbf{g}_3) c_t(\mathbf{k} + \mathbf{g}_1) \right] + \text{h.c.} + (\text{other } \mathbf{k}),
\end{aligned} \tag{S.21}$$

$$\begin{aligned}
H_T(3) &= \int_{-\infty}^{\infty} \frac{d\mathbf{k}}{(2\pi)^2} w c_b^\dagger(\mathbf{k} - \mathbf{g}_3) c_t(\mathbf{k}) + \text{h.c.} \\
&= \int_{\text{MBZ}} \frac{d\mathbf{k}}{(2\pi)^2} w \left[c_b^\dagger(\mathbf{k} - \mathbf{g}_3) c_t(\mathbf{k}) + c_b^\dagger(\mathbf{k} + \mathbf{g}_1) c_t(\mathbf{k} - \mathbf{g}_2) \right] + \text{h.c.} + (\text{other } \mathbf{k}).
\end{aligned} \tag{S.22}$$

Therefore, by keeping the states specified by $\Psi_b(\mathbf{k})$ and $\Psi_t(\mathbf{k})$, we obtain from H_m^+ and H_Δ^+

$$H_\Delta^b = \int_{\text{MBZ}} \frac{d\mathbf{k}}{(2\pi)^2} \Psi_b^\dagger(\mathbf{k}) \begin{pmatrix} 0 & Ve^{-i\psi} & Ve^{+i\psi} \\ Ve^{+i\psi} & 0 & Ve^{-i\psi} \\ Ve^{-i\psi} & Ve^{+i\psi} & 0 \end{pmatrix} \Psi_b(\mathbf{k}) \equiv \int_{\text{MBZ}} \frac{d\mathbf{k}}{(2\pi)^2} \Psi_b^\dagger(\mathbf{k}) h_\Delta^b \Psi_b(\mathbf{k}), \tag{S.23}$$

$$H_\Delta^t = \int_{\text{MBZ}} \frac{d\mathbf{k}}{(2\pi)^2} \Psi_t^\dagger(\mathbf{k}) \begin{pmatrix} 0 & Ve^{+i\psi} & Ve^{-i\psi} \\ Ve^{-i\psi} & 0 & Ve^{+i\psi} \\ Ve^{+i\psi} & Ve^{-i\psi} & 0 \end{pmatrix} \Psi_t(\mathbf{k}) \equiv \int_{\text{MBZ}} \frac{d\mathbf{k}}{(2\pi)^2} \Psi_t^\dagger(\mathbf{k}) h_\Delta^t \Psi_t(\mathbf{k}), \tag{S.24}$$

$$H_T = \int_{\text{MBZ}} \frac{d\mathbf{k}}{(2\pi)^2} \Psi_b^\dagger(\mathbf{k}) \begin{pmatrix} w & 0 & w \\ 0 & w & w \\ w & w & 0 \end{pmatrix} \Psi_t(\mathbf{k}) + \text{h.c.} \equiv \int_{\text{MBZ}} \frac{d\mathbf{k}}{(2\pi)^2} \Psi_b^\dagger(\mathbf{k}) h_{bt} \Psi_t(\mathbf{k}) + \Psi_t^\dagger(\mathbf{k}) h_{tb} \Psi_b(\mathbf{k}). \tag{S.25}$$

Thus, we have rewritten Eq. (S.1) and obtain the moiré wave-number representation as

$$H_{\tau=+} = \int_{\text{MBZ}} \frac{d\mathbf{k}}{(2\pi)^2} (\Psi_b^\dagger(\mathbf{k}), \Psi_t^\dagger(\mathbf{k})) H_{\tau=+}(\mathbf{k}) \begin{pmatrix} \Psi_b(\mathbf{k}) \\ \Psi_t(\mathbf{k}) \end{pmatrix}, \tag{S.26}$$

$$H_{\tau=+}(\mathbf{k}) \equiv \begin{pmatrix} h_m^b(\mathbf{k}) + h_\Delta^b & h_{bt} \\ h_{tb} & h_m^t(\mathbf{k}) + h_\Delta^t \end{pmatrix}. \tag{S.27}$$

We can also obtain that for $\tau = -$ and the BdG Hamiltonian in the same way. In particular, in the presence of spatially uniform pseudo-gauge field \mathbf{A}_s , we can replace $h_m^l(\mathbf{k}) \rightarrow h_m^l(\mathbf{k} + \tau \mathbf{A}_s)$ and the BdG Hamiltonian reads

$$H_{\text{BdG}}(\mathbf{k}, \mathbf{A}_s) = \begin{pmatrix} H_+(\mathbf{k} + \mathbf{A}_s) & \Delta(\mathbf{k}) \\ \Delta(\mathbf{k})^\dagger & -H_-^T(-\mathbf{k} - \mathbf{A}_s) \end{pmatrix}. \tag{S.28}$$

In the main text, we assume that $\Delta(\mathbf{k})$ does not directly couple to \mathbf{A}_s for simplicity, while it actually can. Such effects can formally be incorporated as the vertex corrections to response functions. This requires to microscopically identify the pairing interaction and study how it is affected by SAWs, which go beyond the scope of our work. Instead, we briefly comment on what is expected in the following. The effect of \mathbf{A}_s on $\Delta(\mathbf{k})$ is classified into that of amplitude $\Delta(T)$ and that of form factor, namely $\hat{1}(k_x^2 - k_y^2)/k^2$ and $\hat{1}[(k_x^2 - k_y^2) + 2ik_x k_y]/k^2$ for nematic and chiral d -wave states, respectively, where $\hat{1}$ stands for the identity matrix. The former contribution corresponds to the Higgs mode, and we leave it as the future issue by focusing on the quasiparticle contributions. As for the latter effect, we expect that it may not be significant. Indeed, if SAWs couple as $\Delta(\mathbf{k}) \rightarrow \Delta(\mathbf{k} + \frac{e}{\hbar} \mathbf{A}_s)$, for example, the resulting change in the expression of $\sigma_{\text{inj}}^{x;xx}$ is obtained by replacing $G_{ab}^{\beta\gamma}$ in

$$\sigma_{\text{inj}}^{\alpha;\beta\gamma} = -\frac{e^2 \pi}{2\hbar \Gamma} \int \frac{d^2 \mathbf{k}}{(2\pi)^2} \sum_{a,b} (\mathcal{J}_{aa}^\alpha - \mathcal{J}_{bb}^\alpha) G_{ab}^{\beta\gamma} F_{ab}(\Omega). \tag{S.29}$$

with the true band-resolved quantum metric of the BdG Hamiltonian. As commented on in the main text, this replacement makes only a tiny quantitative change. This seems to be a general feature to some extent, considering that the coupling of \mathbf{A}_s to the normal-state part gives rise to the Fermi velocity $\partial_{\mathbf{k}}\epsilon_{\mathbf{k}}/\hbar$ in the band-resolved quantum metric, which should be compared with e.g., $\partial_{\mathbf{k}}\Delta(\mathbf{k})/\hbar$ for the contribution stemming from the SAWs corrections to the form factor.

We determined the value of the scattering rate Γ in the following way. According to Ref. [2], the mean-free path and the coherence length are $l = 229$ nm and $\xi_0 = 57$ nm, where $l \gg \xi_0$ indicates that the system is in the clean limit. By assuming the relations $\xi_0 = \hbar v_F/\pi\Delta_0$, $l = v_F/\Gamma_N$, and using a typical value of the Fermi velocity v_F , we obtain the normal-state scattering rate as $\Gamma_N \sim 50.5 \mu\text{eV}$, which amounts to $\sim \Delta_0/2$. The scattering rate in the superconducting state would be smaller than Γ_N due to the gap opening, and thus we phenomenologically assume a smaller value $\Gamma = \Delta_0/10 < \Gamma_N$.

SAGE FOR THE SINGLE-BAND MODEL

To understand the behavior of $\sigma_{\text{inj}}^{\alpha;\beta\gamma}$, we illustrate it by simplifying Eq. (S.29) with keeping single band $\epsilon_{\mathbf{k}}$ near the Fermi energy and assuming that a constant order parameter Δ_0 . For simplicity, we keep only $O(Q)$ contributions, while higher-order contributions are important when Q^{-1} and the coherence length ξ_0 are comparable, and are kept in the model calculations. The BdG Hamiltonian Eq. (S.28) reduces to $H_{\text{BdG}}(\mathbf{k}) = \epsilon_{\mathbf{k}}\tau_z + \Delta_0\tau_x$ with Pauli matrices τ_i , when the time-reversal symmetry is preserved in the normal state. Then, $\sigma_{\text{inj}}^{\alpha;\beta\gamma}$ at $T = 0$ recasts into

$$\sigma_{\text{inj}}^{\alpha;\beta\gamma} \simeq -\frac{e^3\pi}{2\Gamma} \int \frac{d^2\mathbf{k}}{(2\pi)^2} \frac{1}{m_{\mathbf{k}}^{\alpha\alpha'}} Q^{\alpha'} G^{\beta\gamma}(\mathbf{k}) \delta(\hbar\Omega - 2E_{\mathbf{k}}). \quad (\text{S.30})$$

Here, we have defined $G^{\beta\gamma}(\mathbf{k}) = \hbar v_{\mathbf{k}}^{\beta} \hbar v_{\mathbf{k}}^{\gamma} |\Delta_0|^2 / 4E_{\mathbf{k}}^4$, $E_{\mathbf{k}} = \sqrt{\epsilon_{\mathbf{k}}^2 + |\Delta_0|^2}$, $v_{\mathbf{k}}^{\beta} = \partial\epsilon_{\mathbf{k}}/\hbar\partial k^{\beta}$ and $1/m_{\mathbf{k}}^{\alpha\alpha'} = \partial^2\epsilon_{\mathbf{k}}/\hbar^2\partial k^{\alpha}\partial k^{\alpha'}$.

We can estimate the magnitude of $\sigma_{\text{inj}}^{\alpha;\beta\gamma}$ by considering a parabolic band $\epsilon_{\mathbf{k}} = \hbar^2 k^2/2m - \mu$. In this case, Eq. (S.30) is a positive or negative definite tensor depending on the sign of the effective mass m , and we obtain $\sigma_{\text{inj}}^{\alpha;\beta\gamma} = -s \frac{e^3\pi^2}{64\eta\hbar^2} \frac{\xi_0^2 Q^{\alpha} \delta_{\beta\gamma}}{\tilde{\Omega}^3 \sqrt{\tilde{\Omega}^2 - 1}} \theta(\tilde{\Omega} - 1)$ with the Heaviside step function $\theta(x)$. Here, we defined $s = \text{sgn}[m] = \text{sgn}[\mu]$, the dimensionless frequency $\tilde{\Omega} = \hbar\Omega/2|\Delta_0|$, and the coherence length $\xi_0 = \frac{\hbar\sqrt{2\mu/m}}{\pi|\Delta_0|}$. Thus, a finite $\sigma_{\text{inj}}^{\alpha;\beta\gamma}$ of the order of $\xi_0^2 Q/\eta$ is expected regardless of the pairing symmetry.

SAGE FOR CHIRAL/NEMATIC p -WAVE STATES

In this section we analyze the SAGE for chiral and nematic p -wave states, whose order parameters are assumed to be $\Delta(\mathbf{k}) = \Delta(T)(k_x + ik_y)/k$ and $\Delta(\mathbf{k}) = \Delta(T)k_x$, respectively. We show the numerical results in Fig. S1. The qualitative behavior of the JDOS, SAGE, and the nematicity is consistent with that of d -wave states since SAGE reflect the underlying gap structure. Strictly speaking, tWSe₂ lacks the inversion symmetry due to a finite displacement field which allows parity mixing [3, 4]. Nevertheless, even when parity mixing is included, the gap topology of the chiral $p+d$ and nematic $p+d$ states is qualitatively the same—namely, full-gap and nodal structure—and so are their SAGE responses. These results indicate that SAGE can serve as a sensitive probe for both chiral and nematic states.

PEAK STRUCTURE OF SAGE IN LOW-FREQUENCY REGIME

In this section, we examine the origin of the low-frequency peak in the acoustogalvanic conductivity. This is a common feature appears in the nematic p - and d -wave states, and to be specific, here we focus on the nematic d -wave state at $\varphi = 2\pi/3$. In Fig. S2, we show the numerical results of the acoustogalvanic conductivity σ_{inj}^L for the nematic d -wave state with $\varphi = 2\pi/3$ and the normal state. The low-frequency peak similar to that of the nematic state is reproduced in the normal state, and thus that of the nematic state would be understood as a reminiscent of the normal-state response. The peak structure is obtained both in the cases of fixed Q and $Q = \Omega/c_t\xi$.

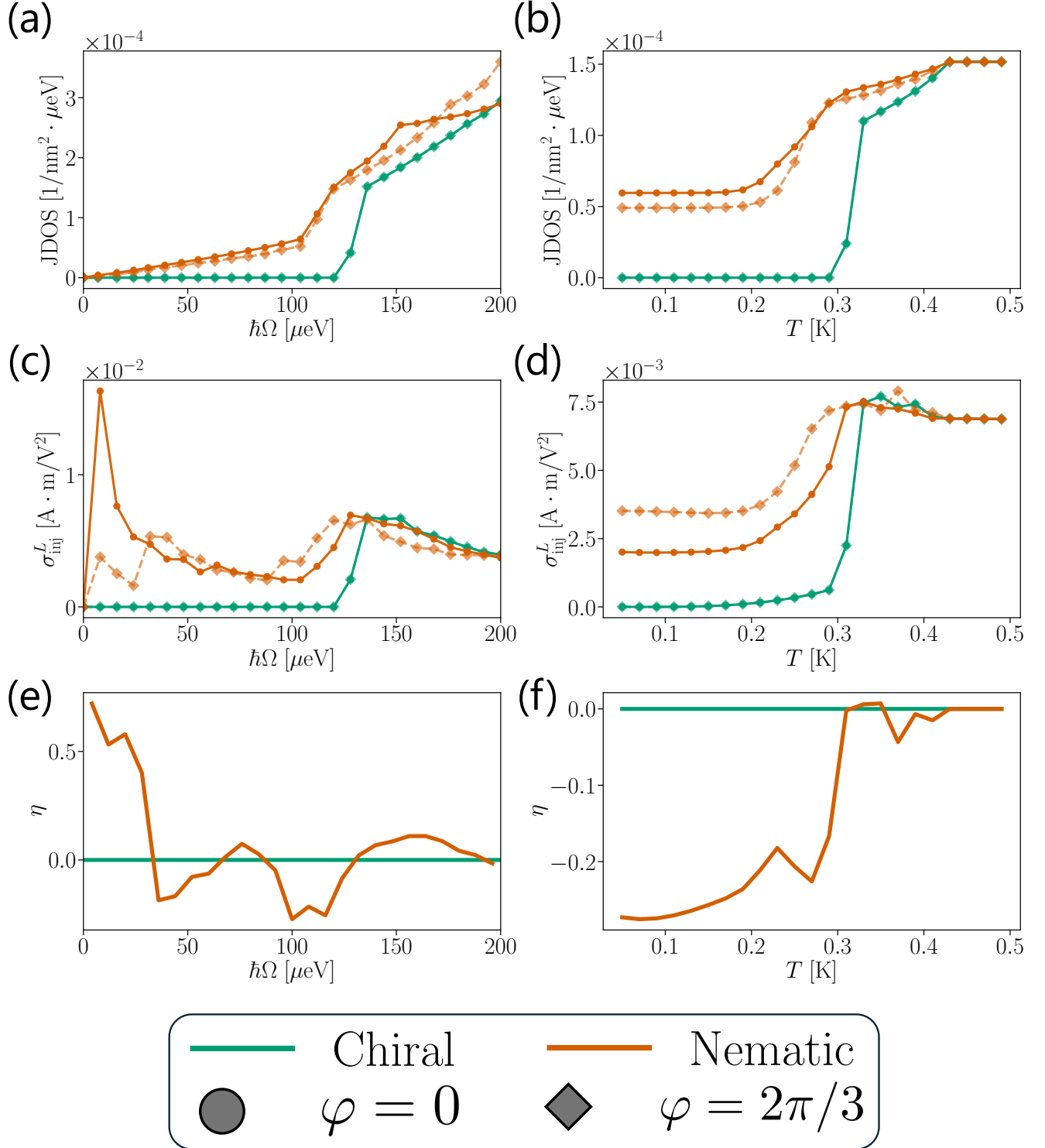


FIG. S1. (a),(c) and (e) Frequency and (b),(d) and (f) temperature dependencies of SAGE in chiral/nematic p -wave states. (a) and (b) show the JDOS, (c) and (d) the acoustogalvanic conductivity, and (e) and (f) the nematicity of the acoustogalvanic conductivity. The green curves correspond to the chiral and orange curves correspond to the nematic states, respectively, while disks and squares represent $\varphi = 0$ and $\varphi = 2\pi/3$. The results for chiral states with $\varphi = 0$ and $\varphi = 2\pi/3$ coincide as ensured by symmetry.

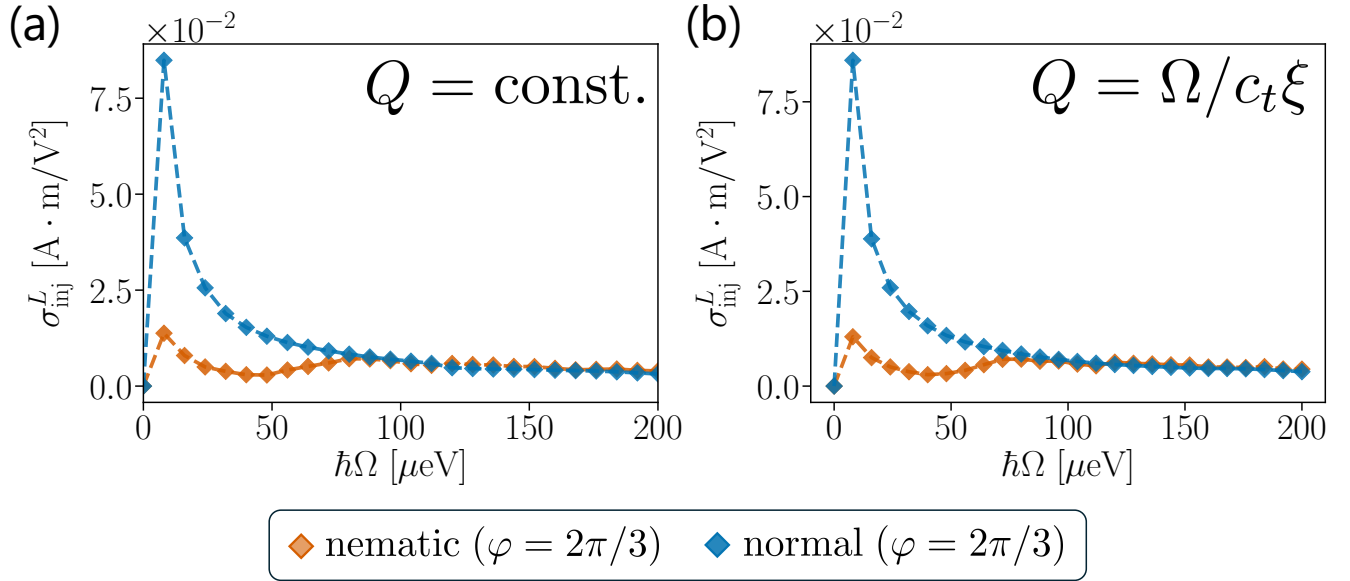


FIG. S2. Acoustogalvanic conductivity σ_{inj}^L for the nematic d -wave state with $\varphi = 2\pi/3$ (orange) and the normal state (blue). Throughout this Letter, the normal state is defined by setting $\Delta = 0$ in the BdG Hamiltonian. Panels (a) and (b) show the results with fixed Q and $Q = \Omega/c_t\xi$, respectively.

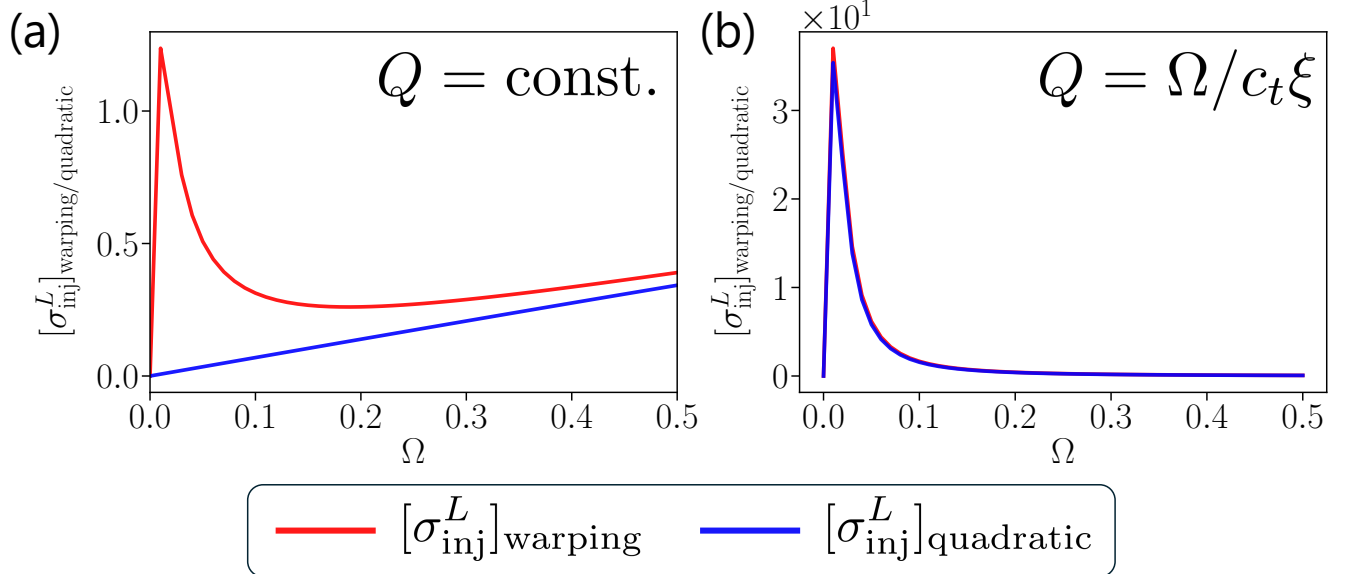


FIG. S3. Acoustogalvanic conductivity σ_{inj}^L with single band model $H_{\text{BdG}} = \epsilon_{\mathbf{k}}\tau_z$, where $\epsilon_{\mathbf{k}} = (k_x^2 + k_y^2)/2m + w(k_x^3 - 3k_xk_y^2) - \mu$ (red), $\epsilon_{\mathbf{k}} = (k_x^2 + k_y^2)/2m - \mu$ (blue) and $(m, w, \mu) = (0.05, 3, 1)$. Panels (a) and (b) show the results with fixed Q and $Q = \Omega/c_t\xi$, respectively.

To understand the low-frequency behavior of $\sigma_{\text{inj}}^{\alpha;\beta\gamma}$ in the normal state, we set $T = 0$ and consider the normal-state BdG Hamiltonian for the single-band model, $H_{\text{BdG}} = \epsilon_{\mathbf{k}}\tau_z$. In this case, we obtain

$$\sigma_{\text{inj}}^{\alpha;\beta\gamma} = -\frac{1}{2} \frac{e^3 \pi}{2\hbar\Gamma} \int \frac{d^2 k}{(2\pi)^2} (v_{\mathbf{k}+\frac{\mathbf{Q}}{2}}^\alpha - v_{\mathbf{k}-\frac{\mathbf{Q}}{2}}^\alpha) g_s^{\beta\gamma}(\mathbf{k}) F_{\mathbf{k}}(\Omega), \quad (\text{S.31})$$

with

$$g_s^{\beta\gamma}(\mathbf{k}) = \frac{\hbar\bar{v}_{\mathbf{k},\mathbf{Q}}^{\beta}\hbar\bar{v}_{\mathbf{k},\mathbf{Q}}^{\gamma}}{(\epsilon_{\mathbf{k}+\frac{\mathbf{Q}}{2}} - \epsilon_{\mathbf{k}-\frac{\mathbf{Q}}{2}})^2}, \quad F_{\mathbf{k}}(\Omega) = \sum_{s=\pm 1} [\theta(-s\epsilon_{\mathbf{k}+\frac{\mathbf{Q}}{2}}) - \theta(-s\epsilon_{\mathbf{k}-\frac{\mathbf{Q}}{2}})]\delta(\hbar\Omega - s\epsilon_{\mathbf{k}+\frac{\mathbf{Q}}{2}} + s\epsilon_{\mathbf{k}-\frac{\mathbf{Q}}{2}}), \quad (\text{S.32})$$

$v_{\mathbf{k}}^{\alpha} = \partial_{k_{\alpha}}\epsilon_{\mathbf{k}}/\hbar$, and $\bar{v}_{\mathbf{k},\mathbf{Q}}^{\beta} = (v_{\mathbf{k}+\mathbf{Q}/2}^{\beta} + v_{\mathbf{k}-\mathbf{Q}/2}^{\beta})/2$. Here, $g_s^{\beta\gamma}(\mathbf{k})$ is the normal-state counterpart of the pseudo-gauge-field quantum metric $G_{ab}^{\beta\gamma}$, which is generally nontrivial even for the single-band metal due to the finite momentum transfer \mathbf{Q} . Note that $F_{\mathbf{k}}(\Omega)$ vanishes as $\Omega \rightarrow 0$, and therefore the region near the crossing points of the two shifted Fermi surfaces $\epsilon_{\mathbf{k}+\mathbf{Q}/2} = 0$ and $\epsilon_{\mathbf{k}-\mathbf{Q}/2} = 0$ contribute to the integral when Ω is small. If we denote such crossing points by \mathbf{k}_* , we may approximate $\sigma_{\text{inj}}^{\alpha;\beta\gamma}$ by

$$\sigma_{\text{inj}}^{\alpha;\beta\gamma} \simeq -\frac{e^3\pi}{4\hbar\Gamma} \sum_{\mathbf{k}_*} (v_{\mathbf{k}_*+\frac{\mathbf{Q}}{2}}^{\alpha} - v_{\mathbf{k}_*-\frac{\mathbf{Q}}{2}}^{\alpha}) \frac{\bar{v}_{\mathbf{k}_*,\mathbf{Q}}^{\beta}\bar{v}_{\mathbf{k}_*,\mathbf{Q}}^{\gamma}}{\Omega^2} \int_{\mathbf{k} \sim \mathbf{k}_*} \frac{d^2k}{(2\pi)^2} F_{\mathbf{k}}(\Omega). \quad (\text{S.33})$$

Thus, as long as the prefactor of the integral is finite, we obtain a divergent acoustogalvanic effect of $O(1/\Omega)$ since $\int \frac{d^2k}{(2\pi)^2} F_{\mathbf{k}}(\Omega) = O(\Omega)$ as understood from $\lim_{\Omega \rightarrow 0} F_{\mathbf{k}}(\Omega) = 0$. This reproduces the obtained divergent normal-state $\sigma_{\text{inj}}^{\alpha;\beta\gamma}$ obtained for tWSe₂. Note that the behavior of $\sigma_{\text{inj}}^L \rightarrow 0$ as $\Omega \rightarrow 0$ obtained in the numerical calculations is due to the replacement of the delta functions with a finite-width Gaussian distribution.

We note that anharmonicity of the band dispersion is required to see such a divergent acoustogalvanic conductivity in the longitudinal component $\sigma_{\text{inj}}^L = \hat{Q}^{\alpha}\sigma_{\text{inj}}^{\alpha;\beta\gamma}\hat{Q}^{\beta}\hat{Q}^{\gamma}$. Indeed, in the case of a quadratic band dispersion, we have $\bar{v}_{\mathbf{k}_*,\mathbf{Q}}^{\beta}\hat{Q}^{\beta} = (\epsilon_{\mathbf{k}_*+\frac{\mathbf{Q}}{2}} - \epsilon_{\mathbf{k}_*-\frac{\mathbf{Q}}{2}})/\hbar Q$, which vanishes by definition of \mathbf{k}_* . In this case, we have $\hat{Q}^{\beta}\hat{Q}^{\gamma}g_s^{\beta\gamma}(\mathbf{k})F_{\mathbf{k}}(\Omega) = \frac{1}{Q^2}F_{\mathbf{k}}(\Omega)$, and we obtain

$$[\sigma_{\text{inj}}^L]_{\text{quadratic}} = -\frac{e^3\pi}{4\Gamma Q} \frac{1}{m\hat{Q}\hat{Q}} \int \frac{d^2k}{(2\pi)^2} F_{\mathbf{k}}(\Omega), \quad \frac{1}{m\hat{Q}\hat{Q}} = \hat{Q}^{\alpha}\hat{Q}^{\alpha'}\partial_{k_{\alpha}}\partial_{k'_{\alpha}}\epsilon_{\mathbf{k}}/\hbar^2. \quad (\text{S.34})$$

This is $O(\Omega)$ as $\Omega \rightarrow 0$. To illustrate how this changes to the $1/\Omega$ divergence, let us consider the system with trigonal warping, $\epsilon_{\mathbf{k}} = \hbar^2\mathbf{k}^2/2m + w(k_x^3 - 3k_xk_y^2) - \mu$, and set $\alpha = \beta = \gamma = x$ and $\mathbf{Q} = Q\hat{x}$. Then, we obtain

$$\hbar\bar{v}_{\mathbf{k},\mathbf{Q}}^x Q = \epsilon_{\mathbf{k}+\frac{\mathbf{Q}}{2}} - \epsilon_{\mathbf{k}-\frac{\mathbf{Q}}{2}} + \frac{1}{2}wQ^3, \quad (\text{S.35})$$

and thus Eq. (S.31) leads to

$$\begin{aligned} [\sigma_{\text{inj}}^{x;xx}]_{\text{warping}} &= -\frac{e^3\hbar\pi}{4\Gamma(\hbar Q)^2(\hbar\Omega)^2} \left((\hbar\Omega)^2 + \frac{w^2}{4}Q^6 \right) \int \frac{d^2k}{(2\pi)^2} \left(\frac{\hbar Q}{m} + \frac{6wk_xQ}{\hbar} \right) F_{\mathbf{k}}(\Omega) \\ &\quad - \frac{e^3\hbar\pi}{4\Gamma(\hbar Q)^2(\hbar\Omega)^2} \sum_{s=\pm 1} s\hbar\Omega Q^3 \int \frac{d^2k}{(2\pi)^2} \left(\frac{\hbar Q}{m} + \frac{6wk_xQ}{\hbar} \right) \\ &\quad \cdot [\theta(-s\epsilon_{\mathbf{k}+\frac{\mathbf{Q}}{2}}) - \theta(-s\epsilon_{\mathbf{k}-\frac{\mathbf{Q}}{2}})]\delta(\hbar\Omega - s\epsilon_{\mathbf{k}+\frac{\mathbf{Q}}{2}} + s\epsilon_{\mathbf{k}-\frac{\mathbf{Q}}{2}}). \end{aligned} \quad (\text{S.36})$$

The integrals give $O(\Omega)$ contributions, and thus, $\sigma_{\text{inj}}^{x;xx}$ becomes $O(1/\Omega)$ owing to the trigonal warping, reproducing the low-frequency divergence.

As illustrated for the system with trigonal warping, the low-frequency divergence of $\sigma_{\text{inj}}^{\alpha;\beta\gamma}$ is originated from that of the pseudo-gauge-field quantum metric $g_s^{\beta\gamma}(\mathbf{k})$ as approaching $\Omega \rightarrow 0$. The longitudinal component of the pseudo-gauge-field quantum metric with the delta function is

$$\hat{Q}^{\beta}\hat{Q}^{\gamma}g_s^{\beta\gamma}(\mathbf{k})\delta(\hbar\Omega - s\delta\epsilon_{\mathbf{k},\mathbf{Q}}) = \frac{1}{Q^2} \left(1 + \frac{\hbar\mathbf{Q} \cdot \bar{v}_{\mathbf{k},\mathbf{Q}} - \delta\epsilon_{\mathbf{k},\mathbf{Q}}}{s\hbar\Omega} \right)^2 \delta(\hbar\Omega - s\delta\epsilon_{\mathbf{k},\mathbf{Q}}), \quad \delta\epsilon_{\mathbf{k},\mathbf{Q}} \equiv \epsilon_{\mathbf{k}+\frac{\mathbf{Q}}{2}} - \epsilon_{\mathbf{k}-\frac{\mathbf{Q}}{2}}, \quad (\text{S.37})$$

indicating the low-frequency divergence for non-quadratic bands $\delta\epsilon_{\mathbf{k}_*,\mathbf{Q}} \neq \mathbf{Q} \cdot \bar{v}_{\mathbf{k}_*,\mathbf{Q}}$.

Note that so far we have discussed the case of $\Omega \rightarrow 0$ with fixing Q . It turns out that the low-frequency divergence is also obtained in the case of $\Omega \rightarrow 0$ with $Q \propto \Omega$. In this case, the $(\hbar\Omega)^2$ term in the parenthesis of Eq. (S.36) in

the first line is dominant, and thus we may consider the case of the quadratic dispersion, i.e., $w = 0$. By directly evaluating Eq. (S.31) in the case of $\epsilon_{\mathbf{k}} = \hbar^2 \mathbf{k}^2 / 2m - \mu$, we obtain

$$[\sigma_{\text{inj}}^L]_{\text{quadratic}} = \frac{e^3 \text{sgn}[Q]}{4\pi\hbar\Gamma(\hbar Q)^2} \left[\sqrt{2m\left(\mu' + \frac{\hbar\Omega}{2}\right)} - \sqrt{2m\left(\mu' - \frac{\hbar\Omega}{2}\right)} \right] \quad (\text{S.38})$$

$$= O(\Omega/Q^2), \quad (\text{S.39})$$

where $\mu' \equiv \frac{m\Omega^2}{2Q^2} + \frac{\hbar^2 Q^2}{8m} + \mu$ and $\mu' - \hbar\Omega/2 \geq 0$. This is again attributed to the divergence of the pseudo-gauge-field quantum metric $\hat{Q}^\beta \hat{Q}^\gamma g_s^{\beta\gamma}(\mathbf{k}) = 1/Q^2$, by noting that $\int \frac{d^2 k}{(2\pi)^2} F_{\mathbf{k}}(\Omega) = O(\Omega/Q)$ as turns out from the above results. These behavior has been confirmed by the numerical calculations, as shown in Fig. S3, where the low-frequency divergence is obtained with the trigonal warping both for $Q = \text{const.}$ and $Q = \Omega/c_t\xi$, while is obtained without it only for $Q = \Omega/c_t\xi$.

* matsumoto.tsugumi.78w@st.kyoto-u.ac.jp

- [1] F. Wu, T. Lovorn, E. Tutuc, I. Martin, and A. H. MacDonald, Topological insulators in twisted transition metal dichalcogenide homobilayers, *Phys. Rev. Lett.* **122**, 086402 (2019).
- [2] Y. Guo, J. Pack, J. Swann, L. Holtzman, M. Cothrine, K. Watanabe, T. Taniguchi, D. G. Mandrus, K. Barmak, J. Hone, A. J. Millis, A. Pasupathy, and C. R. Dean, Superconductivity in 5.0° twisted bilayer WSe₂, *Nature* **637**, 839 (2025).
- [3] C. Schrade and L. Fu, Nematic, chiral, and topological superconductivity in twisted transition metal dichalcogenides, *Phys. Rev. B* **110**, 035143 (2024).
- [4] M. Bélanger, J. Fournier, and D. Sénéchal, Superconductivity in the twisted bilayer transition metal dichalcogenide WSe₂ : A quantum cluster study, *Phys. Rev. B* **106**, 235135 (2022).